Feasibility Study of GBAS/INS and RRAIM for Airport Surface Movement Under Low-Visibility Conditions

Junesol Song, Carl Milner, Heekwon No

Received: 6 May 2022 | Revised: 27 April 2024 | Accepted: 2 September 2024

DOI: 10.33012/navi.673

ORIGINAL ARTICLE

Feasibility Study of GBAS/INS and RRAIM for Airport Surface Movement Under Low-Visibility Conditions

Junesol Song[1] | **Carl Milner**[2] | **Heekwon No**[2]

[1] University of Suwon, South Korea

[2] Ecole Nationale de l'Aviation Civile, Université de Toulouse, France

Correspondence
Junesol Song
17, Wauan-gil, Bongdam-eup, Hwaseong-si, Gyeonggi-do, 18323, South Korea
Email: junesol.song@suwona.ac.kr

Carl Milner
7 Avenue Edouard Belin, 31055, Toulouse, France
Email: milner@recherche.enac.fr

Abstract

Currently, surface movement, encompassing all operations on the airport surface prior to take-off and after landing, cannot be achieved under low-visibility conditions by an aircraft-guidance-only solution. In addition to surface movement radar and Automatic Dependent Surveillance–Broadcast, pilots also rely on signage, lighting and reports/commands from the airport traffic control tower, which are partly based on visual inspection of the airport, to aid in guidance from the runway to the gate. Therefore, low-visibility conditions caused by meteorological effects can significantly affect the continuity of operations on the airport surface. Global navigation satellite systems are considered to overcome these difficulties by enhancing guidance and situational awareness on the airport surface. This paper explores the feasibility of utilizing a ground-based augmentation system, which is potentially available at the airport, an inertial navigation system, and relative receiver autonomous integrity monitoring to support surface movement operations in low-visibility conditions. The paper provides results assessing the compliance of the proposed solution to accuracy and integrity requirements.

Keywords

ground-based augmentation system (GBAS), relative receiver autonomous integrity monitoring (RRAIM), surface movement

1 | INTRODUCTION

To ensure air navigation safety, the Standards and Recommended Practices (SARPs) Annex 10 of the International Civil Aviation Organization (ICAO) define the requirements for each phase of flight up to a category (CAT) III precision approach (ICAO, 2018). Surface movement includes all operations on the airport surface not currently covered by the SARPs. The sub-phases consist of rapid exit taxiway, normal and apron taxiway, taxi lane, and stand lead-in line operations (RTCA, 1999). For surface movement, recommendations and propositions have been discussed for performance requirements, but agreement regarding these recommendations is needed for standardization. The Radio Technical Commission for Aeronautics (RTCA) DO-247 (RTCA, 1999) has derived integrity, continuity, and accuracy requirements based on the recommended layout of the aerodrome addressed in ICAO standards (ICAO, 2016). Schuster and Ochieng (2011) adopted

the requirement for a safe landing in CAT III (ICAO, 2018) while neglecting the pilot risk reduction factor to derive requirements more appropriate for low-visibility conditions. Surface movement requirements have been further refined by using realistic flight technical errors (FTE) provided by Airbus (Montloin, 2014).

Currently, pilots rely on visual aids at the airport and instructions from the control tower, which are usually based on visual inspection. However, this type of guidance can be greatly limited under low-visibility conditions caused by snowstorms or heavy fog. Currently, surface movement radar is available to monitor spacings and identify potential collisions under such circumstances (ICAO, 2004). However, it is known that this approach does not provide the accuracy required to identify or prevent such incidents (Schuster & Ochieng, 2011). To maintain continuity of the airport service under all weather conditions, a global navigation satellite system (GNSS) is considered a key element of an advanced surface movement guidance and control system to enhance airport surface movement.

One of the major challenges for a GNSS to support surface operations is the presence of multipath, which can be caused at the airport by signals reflected from the aircraft frame, surrounding buildings, and the ground surface of the airport. The reception of these indirect signals at the airborne receiver causes ranging errors and degrades the navigation performance. Currently, there is no standardized multipath error model that is compliant with the airport environment (Montloin, 2014; Amielh et al., 2019). In this regard, existing research has primarily focused on developing a range error model associated with multipath. Montloin (2014) modeled the impact of multipath errors by adding a deterministic error caused by the airport ground surface and the aircraft frame and a zero-mean stochastic error caused by the surrounding buildings and gate structures. The proposed model depends on the airport environment and employs a GNSS/inertial reference system/digital elevation map solution to evaluate the navigation performance. The results showed that the surface movement accuracy requirement for taxi lanes was not met, and compliance to the integrity requirement was not achieved. RTCA DO-247 (RTCA, 1999) includes an assessment of ground-based augmentation system (GBAS) compliance to support surface movement operations. The assessment is based on the airborne model developed for a specific airport, the Washington Ronald Reagan National Airport. However, the same accuracy requirement is assumed for the different sub-phases of surface movement; thus, the assessment results for taxi lanes or stand lead-in lines might be optimistic, as more stringent requirements are needed for these sub-phases (Schuster & Ochieng, 2011). In addition, the lateral alert limit of the GBAS precision approach used to assess the integrity performance of surface movement is likely optimistic (RTCA, 1999; Schuster & Ochieng, 2011). To develop an airport-independent multipath model, Amielh et al. (2019) derived the modeling parameters of a first-order Gauss–Markov process to overbound the multipath errors simulated for various scenarios for Class F airports.

Multipath error is the major performance-limiting factor for any operation on the airport surface when GNSS code pseudorange measurements are used, and the impact of multipath error becomes more significant at locations closer to the gate area because of the high density of surrounding objects. Unlike code pseudorange measurements, carrier phase measurements are less susceptible to multipath, and the size of the carrier multipath is limited to a quarter of a wavelength (Groves, 2013), i.e., approximately 5 cm. Therefore, this paper proposes to use carrier phase measurements to mitigate the issue of multipath error during the surface movement phase. In the proposed approach, airborne users apply GBAS corrections

and utilize inertial navigation system (INS) assistance after landing, up until a well-defined transition point outside the region of significant multipath errors and where the GBAS service is available. After this transition point, the navigation mode at the airborne receiver is switched to relative receiver autonomous integrity monitoring (RRAIM) to propagate its position using the time-differenced (TD) carrier phase from the last GBAS/INS solution at the transition point. In this paper, to validate the feasibility of the proposed GBAS/INS+RRAIM solution, compliance with accuracy and integrity requirements is assessed. The GBAS ground subsystem provides integrity to airborne users to support CAT III precision approaches, namely, GBAS Approach Service Type (GAST) D for a single-frequency (SF), single-constellation solution and the proposed GAST F (naming convention under discussion in standardization groups) for a dual-frequency (DF), dual-constellation scenario. To take advantage of the integrity provided by the GBAS, this paper derives the limit of the probability of missed detection (PMD) of the GBAS/INS solution, which is needed to meet surface movement requirements prior to the transition point between GBAS/INS and RRAIM. Under this condition, where the GBAS ground monitor meets the surface movement integrity requirement, additional airborne monitoring to enhance the integrity performance during this operational phase need not be addressed. For an integrity analysis of RRAIM following the transition, conventional RRAIM (Lee & McLaughlin, 2008; Gratton et al., 2010) is extended to consider multiple failures. The compliance of the proposed GBAS/INS+RRAIM solution to the accuracy and integrity requirements is expressed in terms of the maximum allowable nominal differential bias, which may be caused by nominal signal deformation (Macabiau et al., 2015) and is expected to be less than 50 cm (Wong, 2014).

2 | SURFACE MOVEMENT REQUIREMENTS

Requirements for surface movement have been proposed in RTCA DO-247 (RTCA, 1999). The accuracy requirement is based on the airport travel surface design requirement and the airport/aircraft category specifications in ICAO Annex 14 (ICAO, 2016). For the integrity requirement, 10% of the target level of safety (TLS), which is set to 10^{-7} for all flight phases (RTCA, 1999; ICAO, 2004), is allocated to surface movement. Because the TLS requirement is related to fatal accidents, it is converted to a probability of incidents based on historical data. A certain portion of the incident risk is allocated to the guidance function, allocated evenly between continuity and integrity. These risks are further allocated to each sub-phase of surface movement according to the length of the exposure time defined in DO-247 (RTCA, 1999). In addition, the pilot risk reduction is leveraged to account for actions by the pilot that mitigate the risk. Schuster and Ochieng (2011) refined these requirements in two aspects. Firstly, for the derivation of the navigation system error (NSE), the airworthiness requirement for a successful landing is considered. This requirement, which is set to $1 - 1\times10^{-6}$ for CAT III (FAA, 1999; EASA, 2003), can be applied to the probability that the aircraft remains within the travel surface clearance (TSC) of each sub-phase. The TSC corresponds to the margin between the main gear of the aircraft and the taxiway edge (RTCA, 1999). This requirement differs from the RTCA DO-247 approach, which requires that the aircraft be located within half of the TSC with a 95% probability (RTCA, 1999). Because the successful landing targeted in CAT III and the safety in surface movement are determined by assessing whether the aircraft is

TABLE 1
Requirements for Each Surface Movement Sub-Phase for a Class F Airport (Amielh et al., 2019)

	Rapid Exit Taxiway	Taxiway	Apron Taxiway	Taxi Lane	Stand Lead-In Line
95% NSE (m)	1.70	1.70	0.84	0.94	0.56
Continuity Risk	2.5×10^{-5}	2.9×10^{-4}	2.9×10^{-4}	7.25×10^{-5}	7.25×10^{-5}
Integrity Risk	2.5×10^{-9}	2.9×10^{-8}	2.9×10^{-8}	7.25×10^{-9}	7.25×10^{-9}
HAL (m)	5.1	4.7	2.4	2.7	1.5

located within the TSC, we adopt Schuster's approach to derive an NSE requirement. Once this criterion is set, the total system error (TSE) can be derived from the TSC. Because the TSE is based on the NSE, the FTE, and the path definition error (PDE), the NSE can be obtained by using the PDE values recommended in the RTCA DO-247 (RTCA, 1999) and the FTE values from the aircraft manufacturer (Amielh et al., 2019). The second aspect considers the pilot risk reduction. RTCA (RTCA, 1999) assumed that the pilot's action is unable to mitigate the continuity risk in 1 out of 10,000 cases for all sub-phases, the integrity risk in 1 out of 20 cases for the taxi lane and gate area, and 1 out of 10 cases for the remaining phases. Schuster and Ochieng (2011) assumed that the pilot's action cannot mitigate the integrity risk at all under zero-visibility conditions, to which the authors agree and extend conservatively to low-visibility conditions. Table 1 summarizes the requirements computed under these considerations for a Class F airport (Amielh et al., 2019). These requirements are used to evaluate the feasibility of the GBAS/INS+RRAIM solution.

3 | METHODOLOGY FOR ACCURACY AND INTEGRITY ASSESSMENT

A GBAS is an augmentation system installed at an airport to support precision approaches and landing. The in-flight coverage of a GBAS is determined by the very-high-frequency data broadcast (VDB) coverage, which is guaranteed within a service volume of 23 nautical miles (FAA, 2021) and may extend even further in practice. In addition, commercial aircraft are typically equipped with high-grade and high-rate inertial sensors. Therefore, if GBAS/INS integration is adopted, the aircraft's position estimates can be further smoothed. Consequently, once the aircraft enters the coverage region of the GBAS service, it can initiate the GBAS/INS tightly coupled filter to use the converged solution during surface operations. At time t_0, the aircraft switches to RRAIM coasting to prevent its position estimates from being affected by multipath errors. The position of the aircraft can be expressed as follows:

$$\boldsymbol{x}_t = \begin{cases} \boldsymbol{x}_{GBAS/INS,t} & t \le t_0 \quad GBAS/INS \ \ mode \\ \boldsymbol{x}_{GBAS/INS,t_0} + \Delta \boldsymbol{x}_{t_0,t} & t > t_0 \quad RRAIM \ \ mode \end{cases} \tag{1}$$

where $\boldsymbol{x}$ denotes the position vector and the subscripts t and t_0 indicate the current time and coasting period, which equals $t - t_0$. $\Delta \boldsymbol{x}_{t_0,t}$ denotes the position change from t_0 to t, which can be estimated via TD carrier phase measurements. Note that in the RRAIM mode, the position is propagated based on the initial GBAS/INS position at t_0.

3.1 | Integrity Allocation

Integrity must be assured throughout the surface operation, both before and after the transition to RRAIM coasting. The allocation of integrity risk must cover all considered fault modes in both cases. The baseline for integrity risk allocation, used for GBAS CAT I precision approaches, is shown in Figure 1(a) (Pullen, 2012). Modifications of this allocation are presented in Figure 1(b) and (c), which address the GBAS/INS+RRAIM cases for $t < t_0$ and $t \geq t_0$, respectively. An additional branch is included to account for INS failure, which is not addressed in this paper and is left for future work, leveraging DO-384 and considering the short operation times of surface movement. With the integrity risk allocated to INS failure, the remaining integrity risk assigned to GBAS and RRAIM decreases. As a result, a more conservative protection level (PL) is calculated.

The allocation tree is applied for each sub-phase of the surface movement. The tree begins with an allocation to the specific sub-phase, which is then divided into H0, H1, and H2 conditions, representing fault-free, single-reference-receiver failure, and all other conditions, respectively, with allocations of 12.5%, 12.5%, and 37.5%, respectively. The branch for all other conditions encompasses major ground subsystem failures, which are not addressed in this paper as such failures are assumed to be managed by the manufacturer, as well as undetected satellite failures.

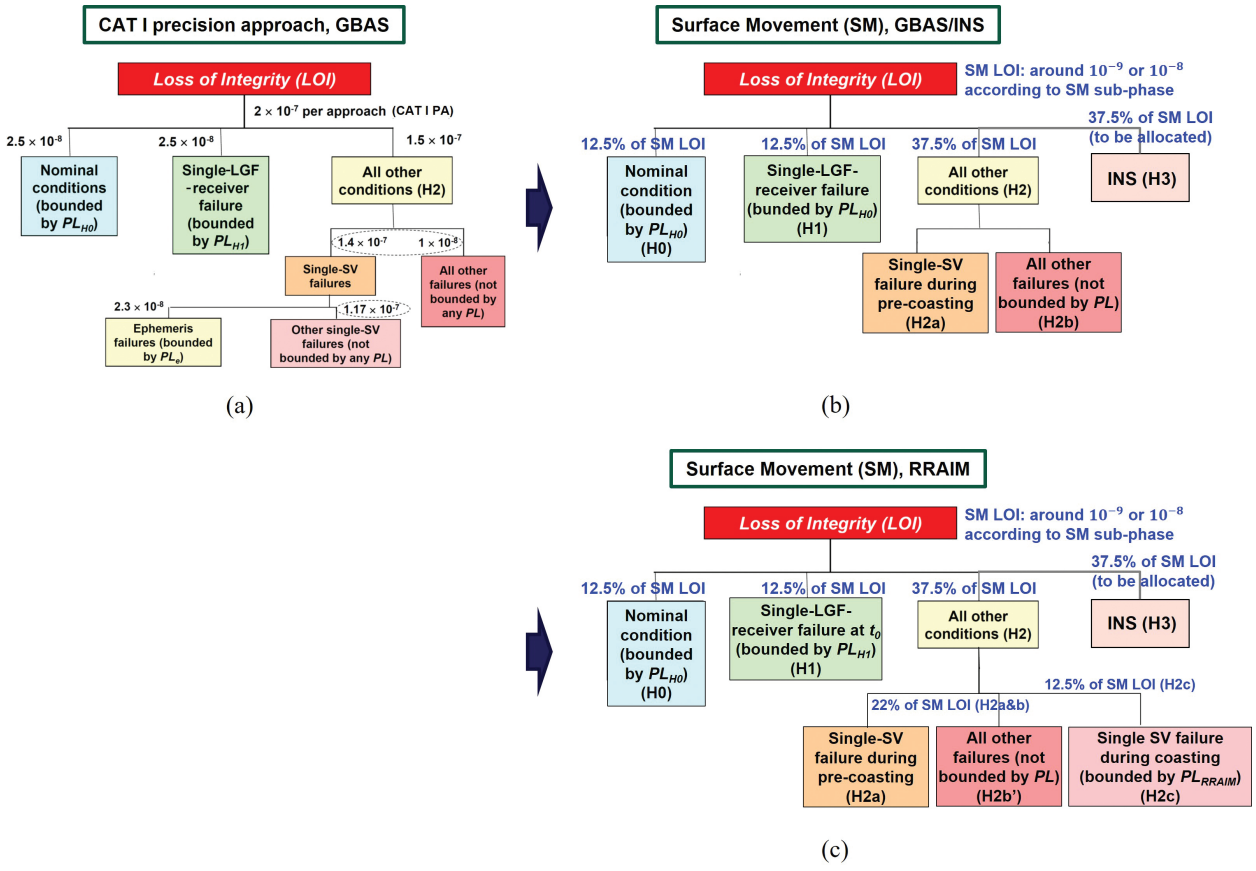

FIGURE 1 (a) Integrity risk allocation for a GBAS CAT 1 precision approach (Pullen, 2012) and (b, c) integrity risk allocation for surface movement (b) during pre-coasting $(t < t_0)$ and (c) during coasting $(t \geq t_0)$
PA: precision approach, SV: space vehicle

To verify whether the solution supports surface movement prior to coasting, $t < t_0$, the requirements defined in Figure 1(b) must be met. These requirements include nominal conditions (H0), receiver failure for a single local area augmentation system ground facility (LGF) (H1), and for all other conditions (H2). The H2 condition is further divided into H2a and H2b, representing single-satellite failures and all other failures, respectively. For the coasting case $t \geq t_0$, the conditions are subdivided depending on the failure conditions of both the GBAS/INS and RRAIM. In Figure 1(c), the nominal condition (H0) accounts for cases in which no failure occurs during either the pre-coasting phase $(t < t_0)$ in GBAS/INS mode or the coasting phase $(t \geq t_0)$ in RRAIM mode. The H1 hypothesis indicates the condition in which the initial position of RRAIM is computed under a single-LGF-receiver failure and no failure has occurred during coasting. All other conditions (H2) include scenarios in which no failure has occurred during pre-coasting $(t < t_0)$, but a single-satellite failure occurred during the coasting period $(t \geq t_0)$ (H2a), as well as situations in which a single satellite is faulty during pre-coasting (H2c). All remaining conditions are denoted as H2b'.

3.2 | Pre-Coasting (GBAS/INS)

The state vector estimate $\hat{\boldsymbol{X}}$ consisting of position and receiver clock $(\delta\tau)$ estimates based on smoothed and GBAS-corrected pseudoranges can be expressed as follows:

$$\hat{\boldsymbol{X}} \equiv \begin{pmatrix} \hat{\boldsymbol{x}} \\ \widehat{\delta\tau} \end{pmatrix} = \left(\boldsymbol{H}^T \boldsymbol{R}^{-1} \boldsymbol{H}\right)^{-1} \boldsymbol{H}^T \boldsymbol{R}^{-1} \boldsymbol{z} \equiv \boldsymbol{S}\boldsymbol{z} \tag{2}$$

$$\boldsymbol{z} \sim N(\boldsymbol{\beta}, \boldsymbol{R}), \qquad \hat{\boldsymbol{X}} \sim N(\boldsymbol{S}\boldsymbol{\beta}, \boldsymbol{Q}) \;\; \textit{where} \;, \boldsymbol{Q} \equiv (\boldsymbol{H}^T \boldsymbol{R}^{-1} \boldsymbol{H})^{-1}$$

where the hat symbol $(\widehat{\blacksquare})$ indicates the estimated value and $\boldsymbol{H}$ and $\boldsymbol{R}$ are the observation and measurement covariance matrices, respectively. The vector $\boldsymbol{z}$ represents the linearized pseudorange residual after GBAS corrections have been applied, and the projection matrix is denoted by $\boldsymbol{S}$. $\boldsymbol{\beta}$ represents the differential nominal bias, which can be caused by nominal signal deformation errors as well as satellite and airborne antenna group delays (Macabiau et al., 2015). Because the airborne antenna group delay is included in the multipath budget and the satellite antenna group delay cancels out when the GBAS correction is applied to the airborne measurement, signal deformation is the main contributor to the nominal bias in the pseudorange residual. The covariance matrix of the estimated solution is denoted by $\boldsymbol{Q}$, which is defined as $(\boldsymbol{H}^T \boldsymbol{R}^{-1} \boldsymbol{H})^{-1}$.

To consider the impact of GBAS/INS tightly coupled integration, the following INS mechanization error equation and measurement equation are used in our analysis (Rhee et al., 2004). In addition, to consider time-correlated errors in the pseudorange residual resulting from GBAS smoothing and correction, the noise of the pseudorange residual is assumed to consist of Gaussian white noise $(\boldsymbol{\varepsilon}_z)$ and colored noise $(\boldsymbol{\xi})$, which can be modeled as a first-order Gauss–Markov process (Khanafseh et al., 2010). The colored noise term is then augmented to the state vector (Crassidis & Junkins, 2004). Thus, the modified system error equation and measurement equation can be expressed as follows:

$$\begin{bmatrix} \delta\dot{\boldsymbol{x}} \\ \delta\dot{\boldsymbol{v}} \\ \delta\dot{\boldsymbol{q}} \\ \delta\dot{\boldsymbol{b}}_a^b \\ \delta\dot{\boldsymbol{b}}_g^b \\ \dot{\delta\tau} \\ \ddot{\delta\tau} \\ \dot{\boldsymbol{\xi}} \end{bmatrix} = \begin{bmatrix} \mathbf{0} & \boldsymbol{I}_{3\times3} & \mathbf{0} & \mathbf{0} & \mathbf{0} & \mathbf{0} & \mathbf{0} & \mathbf{0} \\ \nabla\bar{\boldsymbol{G}}^e - \boldsymbol{\Omega}^2 & -2\boldsymbol{\Omega} & -2\left[C_B^e \bar{F}^b\right]^\times & C_B^e & \mathbf{0} & \mathbf{0} & \mathbf{0} & \mathbf{0} \\ \mathbf{0} & \mathbf{0} & -\boldsymbol{\Omega} & \mathbf{0} & \frac{1}{2}C_B^e & \mathbf{0} & \mathbf{0} & \mathbf{0} \\ \mathbf{0} & \mathbf{0} & \mathbf{0} & \mathbf{0} & \mathbf{0} & \mathbf{0} & \mathbf{0} & \mathbf{0} \\ \mathbf{0} & \mathbf{0} & \mathbf{0} & \mathbf{0} & \mathbf{0} & \mathbf{0} & \mathbf{0} & \mathbf{0} \\ \mathbf{0} & \mathbf{0} & \mathbf{0} & \mathbf{0} & \mathbf{0} & 0 & 1 & 0 \\ \mathbf{0} & \mathbf{0} & \mathbf{0} & \mathbf{0} & \mathbf{0} & 0 & 0 & \mathbf{0} \\ \mathbf{0} & \mathbf{0} & \mathbf{0} & \mathbf{0} & \mathbf{0} & \mathbf{0} & \mathbf{0} & -\frac{1}{\boldsymbol{\tau}_{mp}}\boldsymbol{I}_{n\times n} \end{bmatrix} \begin{bmatrix} \delta\boldsymbol{x} \\ \delta\boldsymbol{v} \\ \delta\boldsymbol{q} \\ \delta\boldsymbol{b}_a^b \\ \delta\boldsymbol{b}_g^b \\ \delta\tau \\ \dot{\delta\tau} \\ \boldsymbol{\xi} \end{bmatrix}$$
$$+ \begin{bmatrix} \mathbf{0} & \mathbf{0} & \mathbf{0} & \mathbf{0} & \mathbf{0} & \mathbf{0} & \mathbf{0} \\ C_B^e & \mathbf{0} & \mathbf{0} & \mathbf{0} & \mathbf{0} & \mathbf{0} & \mathbf{0} \\ \mathbf{0} & \frac{1}{2}C_B^e & \mathbf{0} & \mathbf{0} & \mathbf{0} & \mathbf{0} & \mathbf{0} \\ \mathbf{0} & \mathbf{0} & \boldsymbol{I} & \mathbf{0} & \mathbf{0} & \mathbf{0} & \mathbf{0} \\ \mathbf{0} & \mathbf{0} & \mathbf{0} & \boldsymbol{I} & \mathbf{0} & \mathbf{0} & \mathbf{0} \\ \mathbf{0} & \mathbf{0} & \mathbf{0} & \mathbf{0} & 1 & \mathbf{0} & \mathbf{0} \\ \mathbf{0} & \mathbf{0} & \mathbf{0} & \mathbf{0} & \mathbf{0} & 1 & \mathbf{0} \\ \mathbf{0} & \mathbf{0} & \mathbf{0} & \mathbf{0} & \mathbf{0} & \mathbf{0} & \boldsymbol{I} \end{bmatrix} \begin{bmatrix} \boldsymbol{\omega}_a \\ \boldsymbol{\omega}_g \\ \boldsymbol{\omega}_{ba} \\ \boldsymbol{\omega}_{bg} \\ \omega_{\delta\tau} \\ \omega_{\delta\dot{\tau}} \\ \boldsymbol{\omega}_\xi \end{bmatrix} \tag{3}$$

$$\begin{bmatrix} \boldsymbol{z} \\ \dot{\boldsymbol{z}} \end{bmatrix} = \begin{bmatrix} \boldsymbol{H} & \mathbf{0} & \mathbf{0} & \mathbf{0} & \mathbf{0} & \mathbf{1}_{n\times1} & \mathbf{0} & \boldsymbol{I}_{n\times1} \\ \mathbf{0} & \boldsymbol{H} & \mathbf{0} & \mathbf{0} & \mathbf{0} & \mathbf{0} & \mathbf{1}_{n\times1} & \mathbf{0} \end{bmatrix} \begin{bmatrix} \delta\boldsymbol{x} \\ \delta\boldsymbol{v} \\ \delta\boldsymbol{q} \\ \delta\boldsymbol{b}_a^b \\ \delta\boldsymbol{b}_g^b \\ \delta\tau \\ \dot{\delta\tau} \\ \boldsymbol{\xi} \end{bmatrix} + \begin{bmatrix} \boldsymbol{\varepsilon}_z \\ \boldsymbol{\varepsilon}_{\dot{z}} \end{bmatrix} \tag{4}$$

Here, $\delta\boldsymbol{x}$, $\delta\boldsymbol{v}$, $\delta\boldsymbol{q}$, $\delta\boldsymbol{b}_a$, $\delta\boldsymbol{b}_g$, $\dot{\boldsymbol{z}}$, and $\dot{\delta\tau}$ indicate the position error, velocity error, quaternion error, accelerometer bias error in the body frame, gyro bias error in the body frame, Doppler measurement, and clock drift, respectively. The superscript e denotes the Earth-centered Earth-fixed (ECEF) frame. ω_a, ω_g, ω_{ba}, ω_{bg}, $\omega_{\delta\tau}$, $\omega_{\delta\dot{\tau}}$, and ω_ξ are the process noises of the accelerometer, gyro, accelerometer bias, gyro bias, clock, clock drift errors, and colored noise, respectively. The terms $\nabla\bar{G}^e$, $\bar{F}^b$, C_B^e, and Ω indicate the gradient of the gravitational force, the bias-compensated accelerometer measurement, a transformation matrix from the body to ECEF frame, and the skew symmetric matrix of the Earth's rotation vector, respectively. In addition, τ_{mp} indicates the time constant of the colored noise in the smoothed pseudorange residual error after the GBAS correction has been applied. Because GBAS reference receivers are equipped with a multipath-limiting antenna to reduce multipath errors, temporal correlation mainly arises from multipath in the smoothed pseudorange of the aircraft. Although determining the exact time constant of multipath in the smoothed code is challenging, it is possible to estimate a range of potential time constants in advance (Pervan et al., 2017). Khanafseh et al. (2010) and Langel et al. (2021) have addressed the impact of mismodeling and proposed a covariance bounding method. In particular, to consider the impact of the uncertainty of time constants for colored noise, Langel et al. (2021) proposed a method to ensure that the Kalman filter estimate error covariance bounds the true

estimate error covariance matrix. The authors suggested setting the time constant in the Kalman filter system error equation and the initial variance of the colored noise using the maximum and minimum time constants and the maximum variance of the steady-state colored noise. Our study adopted this method to provide practical results. To obtain the maximum and minimum values of the time constants of smoothed multipath of the aircraft, a Monte Carlo simulation was conducted. According to Pervan et al. (2017), the time constants of raw multipath for Boeing aircraft are 7, 14, and 170 s at the 5th, 50th, and 95th percentiles, respectively. Assuming a log-normal distribution for the time constants, we generated a total of 10^5 time histories of multipath using the first-order Gauss–Markov process. We then applied a carrier smoothing filter to obtain the range of time constants for smoothed multipath. Maximum and minimum time constants of 54 and 2894 s, respectively, were obtained when a carrier smoothing filter with a 100-s time constant was applied. The maximum steady-state variance of multipath is set to the square sum of the receiver models of the GBAS ground station and aircraft (RTCA, 2004; Circiu et al., 2021) because these models provide variances that bound the receiver error after the carrier smoothing filter has been applied. A detailed analysis is provided in Appendix A. The values obtained in Appendix A, which are used in the surface movement simulation, are also shown in Table 2 in Section 4.1.

The benefit of INS integration is a continuous solution, even during GNSS outages; moreover, the solution is smoothed by the high-rate and high-precision INS observations. However, the addition of INS cannot enhance the positioning accuracy in terms of the bias error. Therefore, we assume that the bias error in the GBAS/INS state estimates is equal to that of the GBAS solution, expressed as $\boldsymbol{S\beta}$. To simplify the simulation procedure, only the covariance matrix of the states, denoted as $\boldsymbol{Q}'$, is updated via the discretized Equations (3) and (4). The standard deviations of the GBAS/INS position estimates from $\boldsymbol{Q}'$ are smaller than those from the GBAS-only covariance matrix $\boldsymbol{Q}$ because the use of INS further smooths out the position estimates. The bias error in the position domain, $\boldsymbol{S\beta}$, and the covariance matrix associated with the position and receiver clock errors, denoted as $\boldsymbol{Q}'_{\hat{\boldsymbol{X}}}$, are used to compute the NSE and horizontal PL (HPL) to assess the feasibility of the GBAS/INS pre-coasting solution $(t < t_0)$.

Recall that cases H0, H1, H2a, and H2b must be addressed. For the nominal condition (H0) and the single-LGF-receiver failure condition (H1), the HPL is computed as follows, based on the GBAS PL computation defined in RTCA DO-253D (RTCA, 2017) with the inclusion of an additional nominal bias term, β_{hor}:

$$HPL = \max\left\{HPL_{H0}, \max_j\left(HPL_{H1,j}\right)\right\} \tag{5}$$

$$\text{where } HPL_{H0} = K_{ffmd}\cdot\sqrt{\sum_{i=1}^{n} s_{hor,i}^2\sigma_i^2} + \beta_{hor}$$

$$HPL_{H1,j} = K_{md}\cdot\sqrt{\sum_{i=1}^{n} s_{hor,i}^2\sigma_{i,H1}^2} + \left|\mathrm{B}_{hor,j}\right| + \beta_{hor}$$

The subscripts i and j represent the indices of the satellite and ground reference receiver, respectively. The term s corresponds to the projection coefficient, with $s_{hor} = \sqrt{s_{east}^2 + s_{north}^2}$. σ_i and $\sigma_{i,H1}$ denote the standard deviations of the pseudorange residual of satellite i under the nominal and single-LGF-failure conditions, respectively. $\mathrm{B}_{hor,j}$ represents the position domain B-value in the horizontal direction to account for the impact of a possible LGF receiver failure at the aircraft. This term can be computed as $\sum_{i=1}^{n} s_{hor,i}\mathrm{B}_{value,i,j}$. The B-value, $\mathrm{B}_{value,i,j}$, is broadcast from the ground subsystem through type 1 and 11 GBAS messages. For simulation

purposes, we considered the impact of the B-value and the nominal bias comprehensively by using β_{hor} for different levels of nominal bias. The constants K_{ffmd} and K_{md} represent the multiplier for a fault-free missed detection and a receiver-fault missed detection probability, respectively. These terms are computed based on the approach provided in RTCA DO-245 (RTCA, 2004), assuming that there are four ground receivers and using the continuity and integrity risk requirements for surface movement. For example, $K_{ffmd} = 6.54$ and $K_{md} = 4.06$ are used for a rapid exit taxiway. The term β_{hor} signifies the worst-case impact of the nominal bias in the horizontal domain, computed as follows (van Graas & Soloviev, 2004):

$$\beta_{hor} = \beta_{max}\sqrt{\left(\sum_{i=1}^{n}\left|s_{east,i}\right|\right)^2 + \left(\sum_{i=1}^{n}\left|s_{north,i}\right|\right)^2} \tag{6}$$

where β_{max} indicates the maximum magnitude of the nominal bias. The computed HPL for each sub-phase of surface movement from Equation (5) can be compared with the horizontal alert limit (HAL) derived in Table 1 to assess the feasibility of the GBAS/INS approach.

Next, we must examine the compliance to the integrity risk requirement for the remaining condition, referred to as H2a, which considers the case in which a single-satellite failure occurred during the pre-coasting period. The integrity risk, or equivalently, the probability of hazardously misleading information (HMI), for H2a can be expressed as follows:

$$P_{HMI(H2a)} = P\left(\left|pe\right| > TSC \middle| fault\right) P\left(q < Th \middle| fault\right) P\left(fault\right) \tag{7}$$

where pe, TSC, q, and Th are the horizontal position error (HPE), the TSC determined by the recommended layout of the airport, the test statistic, and the threshold of the test statistic, respectively. The probability that the position error exceeds the TSC can be computed via Equation (8) by using the cumulative distribution function of the standard normal distribution Q:

$$P\left(\left|pe\right| > TSC \mid fault\right) = Q\left(-\frac{E_{hor}+\beta_{hor}+TSC}{\sigma_{TSE}}\right) + Q\left(\frac{E_{hor}+\beta_{hor}-TSC}{\sigma_{TSE}}\right) \tag{8}$$

$$\text{where } \sigma_{TSE}^2 = \sigma_{NSE}^2 + \sigma_{FTE}^2 + \sigma_{PDE}^2$$

Here, σ_{TSE} indicates the standard deviation of the TSE, which can be calculated by using the standard deviations of the NSE (GBAS/INS solution), FTE, and PDE, which are defined in the standards and the reference literature (RTCA, 1999; Amielh et al., 2019). The terms E_{hor} and β_{hor} are the bias error in pe caused by the fault and nominal bias, respectively. $P(fault)$ in Equation (7) indicates the probability of fault during pre-coasting or at t_0 for coasting, depending on the operation mode. It is important to note that for GAST D and GAST F ground monitors, only the single-failure case is considered.

To compute the probability of the fault being present at the current time, we must consider the impact of the GBAS ground monitors in the past. Because of the time correlation in the test statistics, it is assumed that a fault present at time t must have occurred after the last independent test, as the probability of two independent missed detections may be neglected. Here, we define this interval as the effective decorrelation time ($\tau_{effective}$). Now, $P(fault)$ can be computed as follows:

$$P(fault) = \frac{r_{fault}}{3600} \times \tau_{effective} \times N_{sat} \tag{9}$$

where r_{fault} and N_{sat} are, respectively, the fault rate expressed per hour and the number of satellites, which is set to 18 according to the capacity of the VDB datalink (ICAO, 2009). The term $\tau_{effective}$ is set to 100 s, according to the temporal correlation analysis of the GBAS ground monitors, as shown in Appendix B.

Finally, the limit of the probability that the test statistics fail to detect the fault, $P_{MD,limit}$, for surface movement can be computed for different fault biases under a given nominal bias error as follows:

$$P_{MD,limit}\left(\left|E_R\right|\right) = P(q < Th \left| fault\right) = min\left[\frac{P_{HMI(H2a)}}{P(\left|pe\right| > TSC \left| fault\right) P(fault)}, 1\right] \tag{10}$$

The range domain fault bias, E_R, can be obtained by dividing the horizontal position domain fault bias, E_{hor}, by the projection coefficient s_{hor}. The term $P_{MD,limit}$ computed from Equation (10) is a derived requirement expressed as a bound of the PMD under the H2a condition for surface movement. GBAS provides monitoring performance in terms of the differential range error for GAST D (ICAO, 2018) and GAST F (SESAR, 2015). In GAST D and F, this PMD requirement is provided according to the range domain bias error, which is derived based on the vertical domain because the effects in the vertical domain result in a more stringent requirement than in the lateral domain, as stated in the SARPs (ICAO, 2009). As we assess the monitoring performance related to the HPE, we map the range domain performance to the horizontal domain using the horizontal projection factors defined by SESAR (2021). If $P_{MD,limit}$ bounds this guaranteed GBAS monitoring performance (expressed as a requirement in the standards but used here as a minimum performance guarantee), we can take advantage of the integrity provided by the GBAS to meet the surface movement requirement. In our simulation, the maximum allowable magnitude of the nominal bias will be determined, which still allows this condition to be met. Then, Equation (10) can be used to account for the undetected fault in the GBAS/INS solution at t_0 included in hypothesis H2a for coasting.

The remaining condition, H2b, includes a major subsystem failure, which is assumed to be managed by the manufacturer and is not addressed in this paper.

3.3 | Coasting (GBAS/INS+RRAIM)

RRAIM was first proposed to support the instrument approach operation known as lateral precision with vertical guidance at 200 feet (LPV-200) (Lee & McLaughlin, 2008). Lee and McLaughlin (2008) proposed to use RRAIM with other integrity-assured systems such as satellite-based augmentation systems (SBASs) that meet the LPV-200 requirement, where RRAIM is used to fill the gap during any possible SBAS integrity outages. In our analysis, a GBAS/INS solution is used with RRAIM at the airport. This study investigates the conditions in terms of the maximum allowable nominal bias and the coasting period duration under which GBAS/INS+RRAIM meets the requirement for each surface movement sub-phase. A complete technical description of RRAIM can be found in the literature (Lee & McLaughlin, 2008; Gratton et al., 2010); this paper describes only the necessary information. As shown in Equation (1), the change in position, $\Delta \boldsymbol{x}_{t_0,t}$, based on the TD carrier phase measurement can be expressed as follows:

$$\begin{aligned}\Delta\phi^i_{t-T,t} \equiv \phi^i_t - \phi^i_{t_0} &= \left(\boldsymbol{r}^i_t - \boldsymbol{x}_t\right)\cdot \boldsymbol{l}^i_t - \left(\boldsymbol{r}^i_{t_0} - \boldsymbol{x}_{t_0}\right)\cdot \boldsymbol{l}^i_{t_0} + \Delta\delta\tau + \Delta f^i + \Delta\varepsilon^i_\phi \\ &= \left(\boldsymbol{r}^i_t \cdot \boldsymbol{l}^i_t - \boldsymbol{r}^i_{t_0} \cdot \boldsymbol{l}^i_{t_0}\right) - \Delta\boldsymbol{x}_{t_0,t} \cdot \boldsymbol{l}^i_t - \boldsymbol{x}_{t_0} \cdot \left(\boldsymbol{l}^i_t - \boldsymbol{l}^i_{t_0}\right) + \Delta\delta\tau + \Delta f^i + \Delta\varepsilon^i_\phi\end{aligned} \tag{11}$$

where Δ indicates the time difference operator and i denotes the index of a satellite. The terms ϕ, $\boldsymbol{r}$, $\boldsymbol{x}$, $\boldsymbol{l}$, and f represent the carrier phase measurement, satellite position, aircraft position, line-of-sight (LOS) vector, and fault bias, respectively. The position $\boldsymbol{x}_{t_0}$ estimated by the GBAS/INS is used to compensate $\boldsymbol{x}_{t_0} \cdot \left(\boldsymbol{l}_t^i - \boldsymbol{l}_{t_0}^i\right)$ in Equation (11). This leads to a propagation of the nominal bias contained in the pseudorange residual to the TD position solution. The covariance matrix and estimation bias $(\Delta\hat{\boldsymbol{X}})$ can be expressed as follows (Lee & McLaughlin, 2008):

$$\boldsymbol{Q}'_{\Delta\hat{X}} \equiv cov\left(\Delta\hat{\boldsymbol{X}}\right) = \boldsymbol{Q}_{\Delta\hat{X}} + \boldsymbol{S}_{\Delta\phi}\Delta\boldsymbol{H}_{t-T,t}\boldsymbol{Q}'_{\hat{X}}\Delta\boldsymbol{H}^{\boldsymbol{T}}_{t_0,t}\boldsymbol{S}^T_{\Delta\phi} \tag{12}$$

$$\Delta\hat{\boldsymbol{X}}_{bias} = \left(\boldsymbol{H}_t^T\boldsymbol{R}_{\Delta\phi}^{-1}\boldsymbol{H}_t\right)^{-1}\boldsymbol{H}_t^T\boldsymbol{R}_{\Delta\phi}^{-1}\left(\Delta\boldsymbol{f} + \Delta\boldsymbol{H}\hat{\boldsymbol{X}}_{bias}\right) = \boldsymbol{S}_{\Delta\phi}\Delta\boldsymbol{f} - \boldsymbol{S}_{\Delta\phi}\Delta\boldsymbol{H}_{t_0,t}\boldsymbol{S}\boldsymbol{\beta} \tag{13}$$

where $\boldsymbol{R}_{\Delta\phi}$ is the measurement covariance of the TD carrier phase and $\boldsymbol{S}_{\Delta\phi}$ indicates the projection coefficient based on the TD observation matrix $\Delta\boldsymbol{H}_{t_0,t}$. Finally, the covariance matrix and bias at time t in Equation (1) can be expressed by Equations (14) and (15):

$$\boldsymbol{Q}_t \equiv cov\left(\boldsymbol{x}_t\right) = \left[\left(\boldsymbol{I} - \boldsymbol{S}_{\Delta\phi}\Delta\boldsymbol{H}_{t_0,t}\right)\boldsymbol{Q}'_{\hat{X}}\left(\boldsymbol{I} - \boldsymbol{S}_{\Delta\phi}\Delta\boldsymbol{H}_{t_0,t}\right)^T + \boldsymbol{Q}_{\Delta\hat{X}}\right]_{(1:3,1:3)} \equiv \boldsymbol{Q}_{RRAIM} \tag{14}$$

$$\boldsymbol{x}_{t,bias} = \left[\left(\boldsymbol{I} - \boldsymbol{S}_{\Delta\phi}\Delta\boldsymbol{H}_{t_0,t}\right)\boldsymbol{S}\boldsymbol{\beta} + \boldsymbol{S}_{\Delta\phi}\Delta\boldsymbol{f}\right]_{(1:3)} = \left[\boldsymbol{M}\boldsymbol{\beta} + \boldsymbol{S}_{\Delta\phi}\Delta\boldsymbol{f}\right]_{(1:3)} \tag{15}$$

The RRAIM HPL can be computed as follows, based on a solution separation (SS) integrity monitoring approach under a single-satellite failure assumption (Lee & McLaughlin, 2008) for a nominal condition (H0), a single-LGF failure (H1), and the single-satellite failure condition (H2c):

$$HPL_{RRAIM} = \max\left\{HPL_{H0}, \max_j\left(HPL_{H1,j}\right), \max_i\left(HPL_{H2c,i}\right)\right\} \tag{16}$$

$$\text{where } HPL_{H0} = k_{FF}\cdot\sqrt{\boldsymbol{Q}_{RRAIM}(1,1) + \boldsymbol{Q}_{RRAIM}(2,2)} + \beta_{hor,RRAIM}$$

$$HPL_{H1,j} = k_{FC}\cdot\sqrt{\boldsymbol{Q}_{RRAIM,H1}(1,1) + \boldsymbol{Q}_{RRAIM,H1}(2,2)} + \left(|\boldsymbol{MS}|B_{value,j}\right)_{hor} + \beta_{hor,RRAIM}$$

$$HPL_{H2c,i} = k_{FC}\cdot\sqrt{\boldsymbol{Q}_{RRAIM,i}(1,1) + \boldsymbol{Q}_{RRAIM,i}(2,2)} + \beta_{hor,i,RRAIM} + Th_{hor,i}$$

For the single-LGF condition (H1), the subscript j denotes the index of the GBAS reference receiver being excluded. Under this condition, the H1 covariance matrix of the GBAS/INS solution is used to compute the covariance matrix of RRAIM, $\boldsymbol{Q}_{RRAIM,H1}$, whilst the impact of the B-value in the RRAIM solution, which can be computed as $|\boldsymbol{MS}|B_{value,j}$, is also included. For the single-satellite failure condition (H2c), the subscript i denotes the satellite that is excluded from the full-set solution to compute the subset solution. Consequently, $\boldsymbol{Q}_{RRAIM,i}$ indicates the covariance matrix of the subset solution of RRAIM with satellite i being excluded. The worst-case impact of a nominal bias on the full-set solution $(\beta_{hor,RRAIM})$ and the subset solutions $(\beta_{hor,i,RRAIM})$ can be computed in the same manner as Equation (6) with different projection matrices $\boldsymbol{M}$ and $\boldsymbol{M_i}$, respectively. $\boldsymbol{M_i}$ is the projection matrix computed with satellite i excluded. The term $Th_{hor,i}$ is the threshold of each SS test statistic when satellite i is excluded. The constants

k_{FF} and k_{FC} are multipliers of fault-free coasting and faulty coasting, which can be computed according to the reference literature using the integrity and continuity risks derived for surface movement requirements (Amielh et al., 2019).

The hypothesis H2b' includes the case in which a fault is not detected by the GBAS ground monitors and is thus present in the GBAS/INS solution at t_0 and is undetected by the RRAIM but impacts the TD solution. Because these monitors are independent, this case is considered highly improbable and may be neglected. To verify the undetected satellite fault in the GBAS/INS solution at t_0 (H2a), $P_{md,limit}$ is assessed by the approach given in Section 3.2.

To consider the impact of multiple simultaneous failures, advanced receiver autonomous integrity monitoring (ARAIM) has been proposed (Blanch et al., 2015). In this paper, we extend RRAIM to consider multiple failures not only for the Global Positioning System (GPS) but also for Galileo by adopting the ARAIM approach. Further details on the derivation of the HPL in ARAIM have been reported by Blanch et al. (2015), and the following equation defined for east or north directions (q) is used in our analysis to compute the RRAIM HPL:

$$2Q\left(\frac{PL_q-\beta_{max}\sum_{j=1}^{n}\left|\boldsymbol{M}_{(q,j)}\right|}{\sqrt{\boldsymbol{Q}_{RRAIM}(q,q)}}\right)+\sum_{k=1}^{N_{fault\ modes}}P_{fault,k}\,Q\left(\frac{PL_q-T_{q,k}-\beta_{max}\sum_{j=1}^{n}\left|\boldsymbol{M}_{\boldsymbol{k}(q,j)}\right|}{\sqrt{\boldsymbol{Q}_{RRAIM,k}(q,q)}}\right)=\frac{1}{2}PHMI\left(1-\frac{P_{not\ monitored}}{PHMI}\right) \quad (17)$$

The term $PHMI$ denotes the probability of an HMI event, which is set to the PHMI allocated to a single-satellite failure in Figure 1(c) for comparison with the results from Equation (16) when a single-satellite failure is considered. We assume that $PHMI$ is halved for the allocation to the east and north components. The term $N_{fault\ modes}$ is the number of possible fault combinations for n satellite faults and a constellation fault per a single constellation. The probability $P_{fault,k}$ is the prior probability of each fault mode k. The term $P_{not\ monitored}$ denotes the sum of the prior probabilities of all fault modes that are not monitored. The PLs in the east and north directions are determined iteratively by Equation (17), and the HPL is computed from the root-sum square of the east and north PLs.

Figure 2 shows the flowchart of the navigation at the aircraft during surface movement based on a GBAS/INS initial position and the RRAIM approach described in this section.

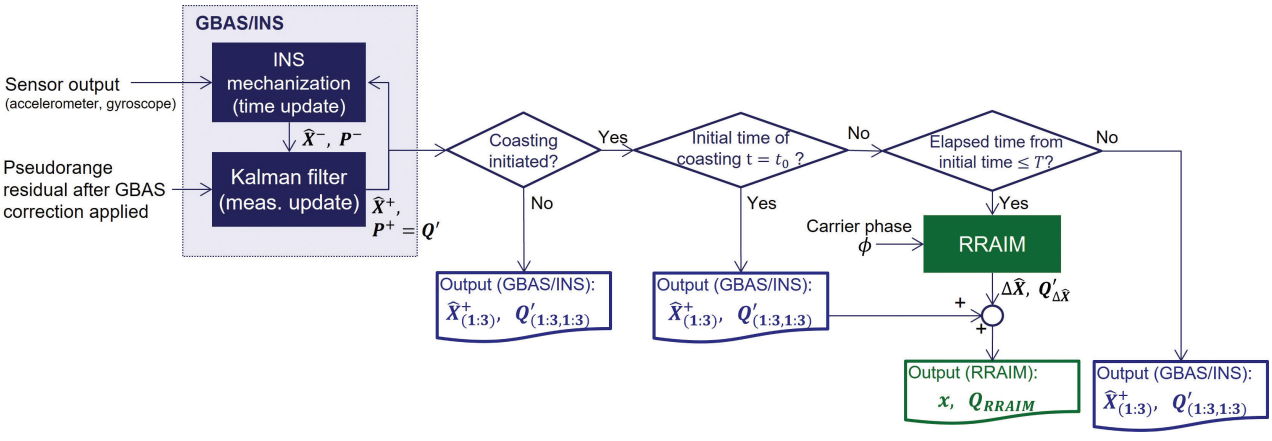

FIGURE 2 Overall methodology of accuracy and integrity assessment

4 | SIMULATION ENVIRONMENT

Figure 3 illustrates the overall feasibility analysis of the GBAS/INS+RRAIM solution for surface movement, which is initiated with a constellation geometry at 10-min intervals. In the figure, the GBAS/INS and RRAIM methodologies described in Section 3 are represented by dark blue and green blocks, respectively. It is worth noting that $\boldsymbol{\beta}'$ represents the range domain nominal bias vector. The vector $\boldsymbol{\beta}$ is the differential nominal bias in the range domain after the GBAS correction has been applied, with each element denoted as β_i. The position domain nominal bias is expressed as $\boldsymbol{S\beta}$. The covariance of the GBAS/INS is denoted as $Q'_{\hat{X}}$ and, when combined with the position domain nominal bias $\boldsymbol{S\beta}$, computes the navigation accuracy and the PL according to the methodologies described in Section 3.2. The covariance matrix $Q'_{\hat{X}}$ and $\boldsymbol{S\beta}$ at t_0 are utilized to compute the RRAIM accuracy and PL. This computation involves a combination of the covariance of the TD carrier phase $R_{\Delta\phi}$, which depends on the coasting time T.

This section presents further details of the error model, the parameters used for simulations, and the simulation scenarios.

4.1 | Measurement Error Models

The standard deviations of the GBAS-corrected pseudorange residual and the TD carrier phase measurements can be expressed as follows:

$$\text{GAST D (SF):}\ \sigma_i^2 = \sigma_{gnd,i}^2 + \sigma_{tropo,i}^2 + \sigma_{iono,i}^2 + \sigma_{air,i}^2 \tag{18}$$

$$\text{GAST F (DF):}\ \sigma_i^2 = \sigma_{gnd,i,IF}^2 + \sigma_{tropo,i}^2 + \sigma_{air,i,IF}^2 \tag{19}$$

$$\text{TD carrier phase (DF):}\ \sigma_{\Delta\phi,i}^2 = \sigma_{\Delta tropo,i}^2 + \sigma_{\Delta clock,i}^2 + 2\sigma_{air,\phi,i,IF}^2 \tag{20}$$

The terms σ_{gnd}, σ_{tropo}, σ_{iono}, and σ_{air} indicate the standard deviations of the ground receiver noise, tropospheric residual, ionospheric residual, and airborne

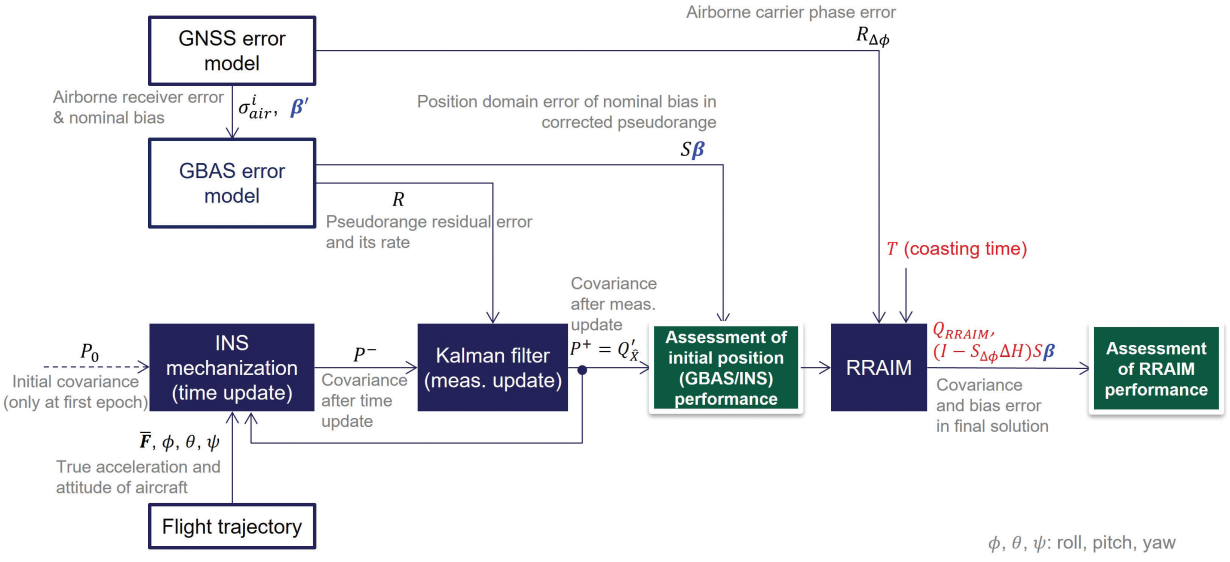

FIGURE 3 Procedure of feasibility analysis of RRAIM based on GBAS/INS

receiver noise, respectively. The subscript i represents the index of a satellite. Note that GAST F uses an ionosphere-free (IF) measurement combination, where the ionospheric delay is eliminated, whereas the receiver noise is inflated by a factor of approximately 2.6 compared with the SF measurement. $\sigma_{\Delta tropo}$, $\sigma_{\Delta clock}$, and $\sigma_{air,\phi}$ are the standard deviations of the spatial decorrelation of the tropospheric delay, the temporal decorrelation of the receiver clock bias, and the carrier phase noise at the airborne receiver, respectively. A scaling factor of $1/20$ is applied to the airborne model so that the standard deviation of the carrier phase noise is conservatively set to approximately 2 cm at an elevation angle of 5°, a factor of 10 greater than the theoretical value achieved by aeronautical-class receivers (Xu, 2007). The variance of the noise in the TD carrier phase is conservatively expressed as twice the variance of the carrier phase noise, assuming no temporal correlation. It is important to note that regardless of the type of GBAS corrections applied, an airborne user can access the DF carrier phase.

Table 2 provides details of the error model described above. The standard deviations of the ground and airborne receiver noise after application of the

TABLE 2
Measurement Error Model and Nominal Bias Error

	Standard deviation model
$\sigma_{gnd,i}$	RTCA DO-245A (RTCA, 2004) $\sigma_{gnd,i,IF}$: an inflation factor, $\frac{\sqrt{\gamma^2+1}}{\gamma-1}$ is applied
$\sigma_{tropo,i}$, $\sigma_{iono,i}$	RTCA DO-245A (RTCA, 2004) • Standard deviation is computed at an elevation of 5° • The distance between the aircraft and the reference point (x_{air}) and the speed of the aircraft (v_{air}) are set to 7 km and 0.042 km/s based on the layout of the Chicago O'Hare airport (one of the largest airports) and the maximum speed at the taxiway (RTCA, 1999) • $\sigma_{vert.iono\,gradient} = 0.004\,mm/km$
$\sigma_{air,i}$, $\sigma_{air,i,IF}$	L1/E1: $0.13+0.17e^{-el/13^\circ}$ (Circiu et al., 2021) IF: $0.34+0.4e^{-el/14^\circ}$ (Circiu et al., 2021)
$\sigma_{air,cp,i,IF}$	$\frac{1}{20}\sigma_{air,i} \approx 2cm$ at $el = 5^\circ$
$\sigma_{\Delta tropo,i}$	$\left[1.22\frac{cm}{km}+0.41\frac{cm}{km}\times\frac{90^\circ-el}{85^\circ}\right]\times v\times T$ (Walter et al., 2008)
$\sigma_{\Delta clock,i}$	$0.085\frac{cm}{s}\times T$ (Walter et al., 2008)
	Differential nominal bias error in pseudorange residual
β_i	[0, 0.1, 0.2, 0.3, 0.4, 0.5] m
	Parameters for overbounding the multipath time constant uncertainty
$\tau_{mp,min}$	30-s carrier smoothing: 26 (Appendix A) 100-s carrier smoothing: 54 (Appendix A)
$\tau_{mp,max}$	30-s smoothing: 2315 (Appendix A) 100-s smoothing: 2894 (Appendix A)
σ^2_{max}	L1/E1: $\sigma^2_{gnd,i}+\sigma^2_{air,i}$ IF: $\sigma^2_{gnd,i,IF}+\sigma^2_{air,i,IF}$

carrier smoothing filter with a 100-s time constant are denoted as σ_{gnd} and σ_{air}, respectively. To estimate the standard deviation of the receiver noise after application of the smoothing filter with a 30-s time constant for GAST D, a factor of $\sqrt{100/30}$ is applied (Murphy et al., 2021). γ, el, and v represent the squared ratio of L1 over L5 frequencies, the elevation angle, and the aircraft speed, respectively. The maximum speed of the aircraft for each sub-phase (RTCA, 1999) is used as v to accurately model the spatial decorrelation of the tropospheric delay. In the simulation, the differential nominal bias varies from 0.1 to 0.5 m with a 0.1-m interval. The largest differential nominal bias is conservatively assumed to be 0.5 m, which is smaller than the recommended value of 0.75 m for absolute nominal bias in ARAIM. It should be noted that the bias error cancels out when the GBAS correction is applied, except for the nominal signal deformation component, which is expected to be less than 0.3 m (Wong, 2014). The parameters $\tau_{mp,max}$, $\tau_{mp,min}$, and σ^2_{max} are used to ensure that the Kalman filter estimate error covariance bounds the true estimate error covariance (Langel et al., 2021). A detailed explanation of these parameters is given in Appendix A.

4.2 | Flight Trajectory and IMU Specifications

To develop the INS mechanization error equation and run the extended Kalman filter (EKF), navigation-grade inertial measurement unit (IMU) sensors are assumed in the simulation. The default sensor performance level is based on the Honeywell HG5700: the 1-sigma bias, the random walk, and the scale factor of the gyro sensor are set to 0.035°/h, 0.006°/√h, and 40 ppm, respectively. In addition, the 1-sigma bias and the scale factor of the accelerometer error are set to 0.035 mg and 120 ppm, respectively. For the process noise of the receiver clock bias and drift, we used Allan variance values for a temperature-compensated crystal oscillator given by Brown and Hwang (1996), and we assumed that the clock dynamic model reflects the actual clock behavior. In our analysis on the accuracy, IMU sensors are considered as fault-free. For the integrity analysis, IMU failure (H3) is considered in the integrity allocation tree; however, its impact is not assessed here, and we leave it as future work.

To simulate the convergence of the covariance matrix of the GBAS/INS, we used the synthesized aircraft waypoints and time information from Wichita to the Chicago airport provided by MATLAB in the sensor fusion and tracking toolbox (MATLAB, 2021). An aircraft trajectory and attitude information at a desired sampling rate are obtained by a generic MATLAB function called "geoTrajectory." In the simulation, 10 Hz and 1 Hz are assumed for the IMU and GNSS outputs, respectively. Figure 4 shows the trajectory of the aircraft in east–north representation and a time history of the height and attitude of the aircraft. The red dotted circle in Figure 4(a) indicates the coverage of the GBAS service.

To test the satellite geometries observed at the GBAS research prototype installed at the Barcelona airport within the Single European Sky ATM Research (SESAR) project, the generated aircraft trajectory in Figure 4 is translated to this location. Satellite geometries were recorded from January 6, 2019 to January 8, 2019 with 10-min intervals. The different initialization times of the GBAS/INS EKF were tested to account for the impact of satellite geometry on the convergence of the covariance matrix.

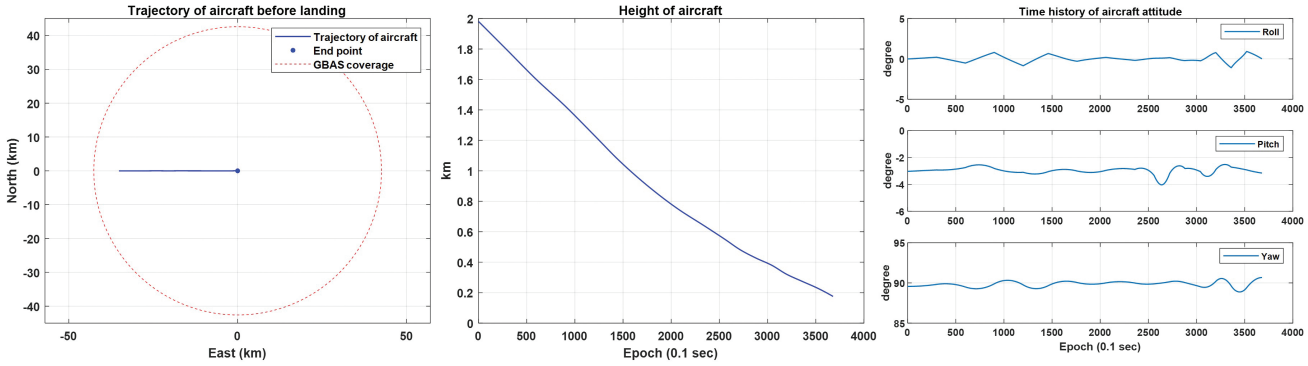

(a) (b) (c)

FIGURE 4 (a) Airborne trajectory represented by east–north axes, (b) time history of aircraft height, and (c) time history of attitude information

TABLE 3
Parameters for HPL Computation

Parameter	Description
$PHMI$	Integrity risk for each sub-phase of surface movement shown in Table 1
P_{sat}, r_{sat}	Prior probability of a satellite fault and the fault rate GPS: $P_{sat}=10^{-5}$, $r_{sat}=10^{-5}/h$ (ICAO, 2018) Galileo: $P_{sat}=3\times10^{-5}$ (Wallner et al., 2021), $r_{sat}=\left[3\times10^{-5}, 10^{-5}\right]/h$
P_{const}	Prior probability of a fault affecting more than one satellite in a constellation GPS: $10^{-8}/h$ (ICAO, 2018), Galileo: $2\times10^{-4}/h$ (Wallner et al., 2021)
P_{Thresh}	Threshold for the integrity risk coming from unmonitored faults, set to the same value as the $PHMI$
P_{FA}	Computed based on the continuity risk derived for each sub-phase of surface movement shown in Table 1

4.3 | Simulation Configuration for Integrity Analysis

The parameters used to compute the HPL are summarized in Table 3. To include multiple-failure modes, the source code from the MATLAB Algorithm Availability Simulation Tool developed by Stanford University was adopted and modified (Stanford University, 2022). The Galileo satellite fault rate, r_{sat}, is set to two possible values in the absence of published values: $r_{sat}=3\times10^{-5}$ (Wallner et al., 2021) when a mean fault duration (MFD) of 1 h is assumed, and $r_{sat}=10^{-5}$ where the GPS value (GPS SPS, 2020) is assumed for Galileo.

5 | SIMULATION RESULTS

Finally, the maximum allowable magnitude of the nominal bias that allows the predicted NSE and HPL to meet the surface movement requirements is assessed. In addition, for an integrity analysis of the pre-coasting solution (GBAS/INS), we investigated the differential nominal bias magnitudes that allow the limit PMD to bound the GBAS monitoring performance. Table 4 details the processing conditions in terms of the measurement frequency and the satellite constellation for the considered simulation scenario.

TABLE 4
GBAS/INS and RRAIM Processing Conditions for Various Simulation Scenarios

	Simulation scenario		
Navigation mode	**GPS-only GAST D**	**GPS-only GAST F**	**GPS/Galileo GAST F**
GBAS/INS	GPS only, SF	GPS only, DF	GPS/Galileo, DF
RRAIM	GPS only, DF	GPS only, DF	GPS/Galileo, DF

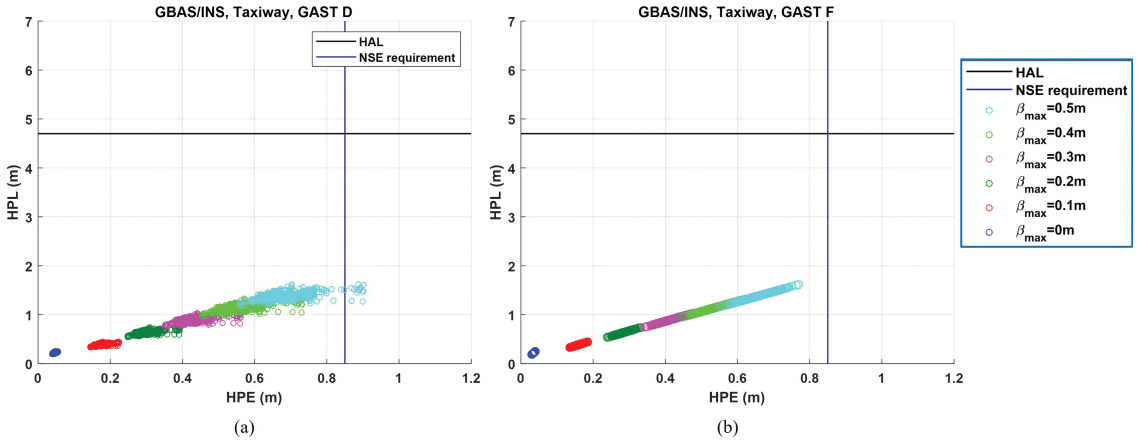

FIGURE 5 HPE and HPL of GBAS/INS during pre-coasting computed for the taxiway using (a) GPS-only GAST D and (b) GPS/Galileo GAST F corrections

5.1 | Pre-Coasting (GBAS/INS) Assessment

A performance assessment of the GBAS/INS during pre-coasting is needed to determine the sub-phase in which RRAIM should be initiated. We expect that the severity of the multipath error will grow as the aircraft approaches the stand lead-in line, but we assess the GBAS/INS performance for all sub-phases and determine the level of allowable differential nominal bias to meet the requirement. Figure 5 shows the HPE against the HPL based on the steady-state covariance matrix from the GBAS/INS tightly coupled filter. Also shown are the NSE requirement and the HAL derived for the taxiway phase. As shown in Figure 5, even with a nominal bias of 0.5 m (cyan), the HPL for both GAST D and F can meet the requirement in the taxiway. In contrast, the HPE is only compliant to the NSE requirement when the magnitude of the nominal bias is less than 0.4 m (light green) for GAST D and 0.5 m (cyan) for GAST F. GAST F allows slightly larger nominal bias values than GAST D because the first-order ionospheric delay residual is completely eliminated in the IF measurement. In addition, despite the performance loss due to the inflated receiver noise in the IF measurement, the improvement in satellite geometry in GPS/Galileo GAST F yields a more significant gain. Table 5 summarizes the maximum allowable nominal bias error for compliance in all sub-phases.

To account for the integrity allocated to the H2a hypothesis, the $P_{md,limit}$ value of the GBAS/INS during pre-coasting is compared with the monitoring performance of the GBAS, which is expressed as the PMD according to the differential fault bias in the range domain, E_R. The limit of the PMD derived for the GBAS/INS during coasting can be expressed as the differential range error, E_R, by using the worst-case projection coefficients in the horizontal direction. These coefficients are set to 2 and 0.7 for GAST D and F (SESAR, 2021), respectively. We also validated these values by simulating all possible satellite geometries observed globally for

TABLE 5
Maximum Allowable Nominal Bias for 100% Compliance to Accuracy and Integrity Requirements for GBAS/INS During Pre-Coasting

GBAS mode	Requirement	Maximum allowable nominal bias (m) for 100% compliance				
		Rapid exit taxiway	Taxiway	Apron taxiway	Taxi lane	Stand lead-in line
GPS-only GAST D	Accuracy	0.4	0.4	0.2	0.2	0.1
	Integrity	0.5	0.5	0.5	0.5	0.4
GPS/ Galileo GAST F	Accuracy	0.5	0.5	0.2	0.2	0.1
	Integrity	0.5	0.5	0.5	0.5	0.4

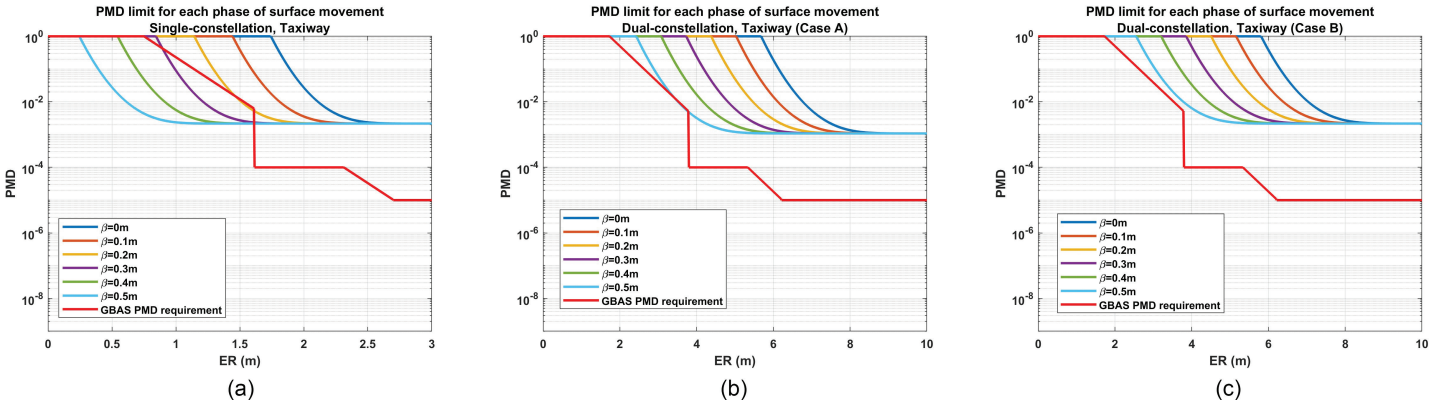

FIGURE 6 PMD limit of GBAS/INS during pre-coasting computed for the taxiway with respect to the GBAS monitoring performance for (a) GAST D, (b) GAST F under Case A ($r_{sat} = 3\times10^{-5}$/h), and (c) GAST F under Case B ($r_{sat} = 1\times10^{-5}$/h)

a duration of 10 days, using the optimized 24 GPS and 24 Galileo constellations (Guilbert, 2016). As mentioned previously, for the satellite fault rate of Galileo, two possible values are considered: 3×10^{-5}/h from the state probability of the Galileo fault, as stated in the draft SARPs (Wallner et al., 2021) under the assumption of a 1-h MFD, and 1×10^{-5}/h, the GPS fault rate. These two cases are denoted by A and B in Figure 6 and Table 6. Figure 6 shows the limit of the PMD, which accounts for the H2a hypothesis, computed for the taxiway with various magnitudes of the differential nominal bias, as well as the GBAS monitoring performance. The results demonstrate that a larger nominal bias is allowed when GAST F is used because of the relaxed GBAS monitoring performance resulting from improved satellite geometry. As mentioned above, the projection factor is greatly improved from 2 to 0.7 when a dual constellation is considered (SESAR, 2021). In addition, case B, which has a smaller Galileo fault rate, allows larger differential nominal biases whilst still bounding the monitoring performance required for the GBAS.

Table 6 summarizes the maximum allowable nominal bias for all sub-phases. It is feasible to use GBAS/INS on the airport surface in the rapid exit taxiway and the taxiway phases, with a sufficient margin in the case of GAST F. For the apron taxiway and taxi lane, the performance is met by GPS/Galileo GAST F with zero nominal bias. From these results, RRAIM based on the GAST D correction should be initiated before the apron taxiway. In the case of GAST F, RRAIM can be initiated at any sub-phase before reaching the stand lead-in line sub-phase.

TABLE 6
Maximum Allowable Nominal Bias for PMD Limit of GBAS/INS During Pre-Coasting to Bound GBAS Monitoring Performance

GBAS mode	Galileo fault rate case	Maximum allowable nominal bias (m) to bound GBAS monitoring performance				
		Rapid exit taxiway	Taxiway	Apron taxiway	Taxi lane	Stand lead-in line
GPS-only GAST D	N/A	0.1	0.1	-	-	-
GPS/ Galileo GAST F	A	0.3	0.4	0	-	-
	B	0.4	0.5	0	0	-

5.2 | Coasting (GBAS/INS+RRAIM) Assessment

In this section, the performance during RRAIM coasting is assessed. Although the results in Section 5.1 introduce some restrictions, we evaluate the performance of RRAIM for all sub-phases. To analyze the degradation of RRAIM performance, coasting times ranging from 10 to 600 s are tested in the simulation. In addition, coasting times longer than the exposure time of each sub-phase of the surface movement operation specified in the standards are also considered, to account for cases in which coasting is started prior to the sub-phase and for possible standby. Figure 7(a) presents the maximum allowable differential nominal bias to ensure full compliance to the 95% NSE and integrity requirements. The white boxes labeled as "NaN" indicate that the requirement is not met even with a differential nominal bias of zero. For a comparative analysis, results for GPS-only GAST D, GPS-only GAST F, and GPS/Galileo GAST F processing modes are shown together. The results suggest that GPS/Galileo GAST F allows the largest differential nominal bias whilst achieving compliance, whereas GPS-only GAST D exhibits slightly better performance than GPS-only GAST F. This observation suggests that the improvement in satellite geometry from GPS/Galileo outweighs the performance loss caused by the inflated noise in the IF measurement. When comparing the results between the SF and DF modes (GPS-only GAST D vs. GPS-only GAST F), the performance loss due to the inflated noise is greater than the loss caused by ionospheric residual error, primarily because the distance between the aircraft and the GBAS reference point at the airport is small.

Figure 7(b) shows the maximum allowable differential nominal bias to ensure that the RRAIM HPL is inferior to the HAL in each sub-phase and for various coasting times under the single-failure assumption. Because only a single-satellite failure is considered and because the prior probabilities of GPS and Galileo satellite fault are almost the same, the magnitude of acceptable nominal bias mainly depends on the satellite geometry and measurement residual errors. Therefore, GPS/Galileo GAST F allows the largest differential nominal bias, preceded by GPS-only GAST D and GPS-only GAST F.

Figure 7(c) summarizes the integrity performance results for a multiple-failure consideration. Compared with the results in Figure 7(b), the allowable differential nominal bias has decreased throughout the parameter space. This result occurs because the integrity risk is allocated to the multiple fault modes in which the subset solution performance is greatly degraded compared with the full-set solution, whilst the HPL must still bound the error with respect to the corresponding PHMI allocation. Under multiple-failure consideration, GPS/Galileo GAST F does

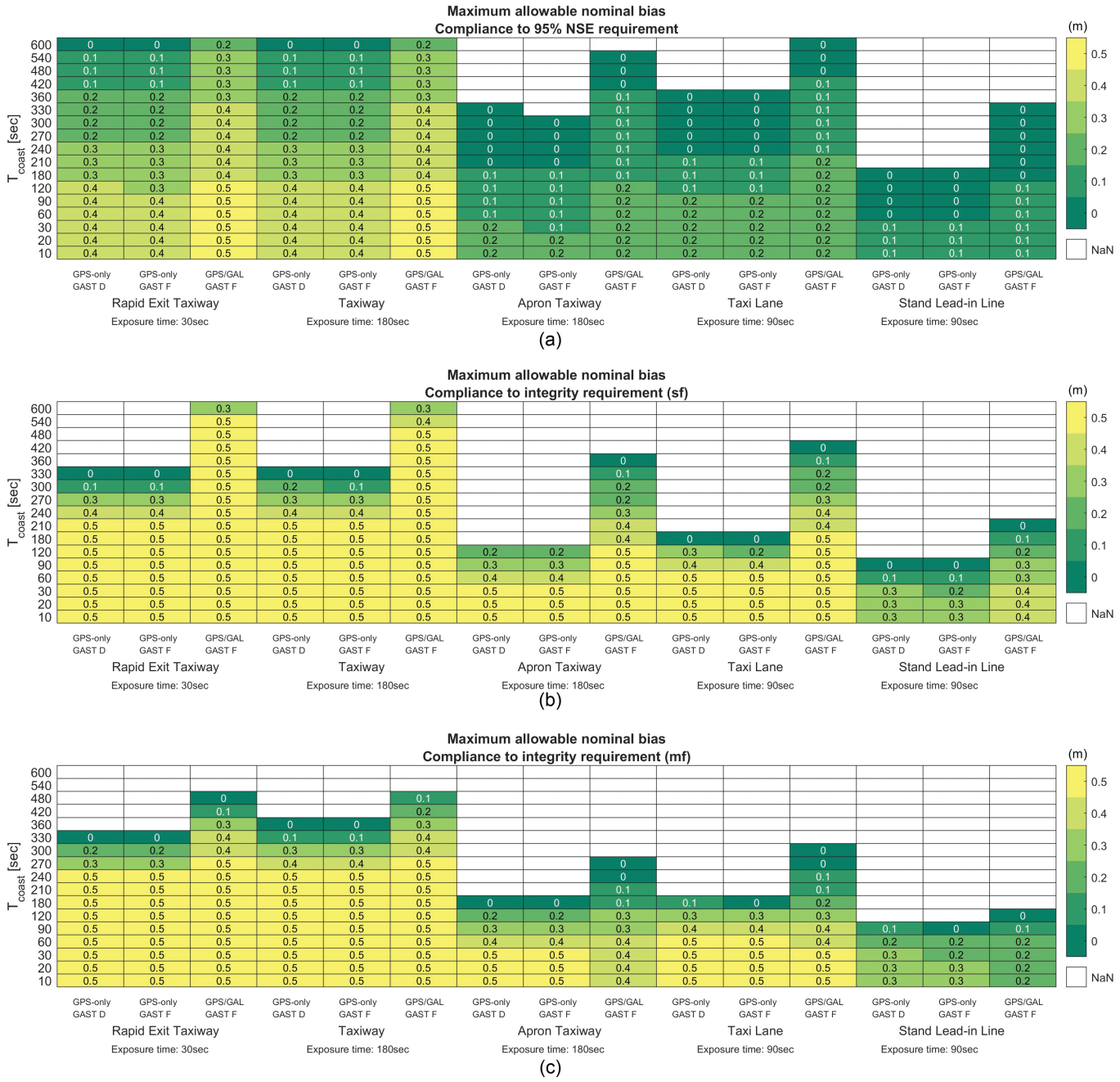

FIGURE 7 Maximum allowable nominal bias (m) for complete compliance to (a) 95% NSE, (b) integrity risk (sf), and (c) integrity (mf) requirements for each sub-phase and GBAS modes
sf: single-failure consideration; mf: multiple-failure consideration

not always allow the largest differential nominal bias. For relatively short coasting times, GPS-only GAST-D allows a larger nominal bias than GPS/Galileo GAST F mode in the stand lead-in line, whereas for larger coasting times, GPS/Galileo GAST F exhibits superior performance. For longer coasting times, the spatial and temporal error decorrelation becomes significant in the SF mode (GAST D); however, in the DF mode (GAST F), the impact is less significant because of the elimination of the ionospheric delay. In contrast, for the apron taxiway with a coasting time of 60 s and for the taxi lane with a coasting time of 20–60 s, GPS-only GAST F allows a slightly larger nominal bias than GPS/Galileo GAST F, even for worse satellite geometry. We attribute this result to the higher prior probability of Galileo constellation fault compared with that of GPS.

TABLE 7
Maximum Allowable Nominal Bias for PMD Limit of GBAS/INS During Coasting to Bound GBAS Monitoring Performance

GBAS mode	Galileo fault rate case	Maximum allowable nominal bias (m) to bound GBAS monitoring performance				
		Rapid exit taxiway	Taxiway	Apron taxiway	Taxi lane	Stand lead-in line
GPS-only GAST D	N/A	0	0.1	-	-	-
GPS/ Galileo GAST F	A	0.3	0.4	0	-	-
	B	0.3	0.5	0	0	-

Table 7 shows the allowable differential nominal bias for $P_{md,limit}$ defined in Equation (9) to meet the integrity risk allocated to the H2b' hypothesis during coasting. The allowable bias is slightly decreased compared with the results during pre-coasting shown in Table 6, resulting from the increased standard deviation of the position estimates due to the spatial and temporal decorrelation errors from RRAIM coasting and the reduced PHMI allocation to the H2 hypothesis during coasting.

6 | DISCUSSION

Extensive simulations have derived the maximum allowable differential nominal bias for which the NSE accuracy and integrity requirements are met, expressed as a function of the coasting period. We have verified that RRAIM coasting using a GBAS/INS initial position can be considered as a potential solution to support low-visibility surface movement operations. This approach is subject to a bound on the nominal bias in the residual pseudorange after the application of GBAS corrections. The literature supports the assumption that this value may be bounded by 0.5 m because of the differential corrections applied by GBAS and is feasibly less than 0.3 m according to Wong (2014).

The other critical performance driver is the achievable coasting period. It remains to be determined at which point the transition to coasting must be performed and when an airport-agnostic approach would be strongly favored. The choice of transition point may be aided by the results presented herein. Although it may not be possible to reach the stand lead-in line, based on the results shown in Table 6, Table 7, and Figure 7, an integrity solution capable of bringing the aircraft to the apron under low-visibility conditions with a possible transition point at the taxiway presents a major operational benefit compared with the delays encountered under current operations without the need for unproven technologies (lidar, camera, etc.).

It should be noted that RRAIM assumes that cycle slips do not occur during the coasting period, given that RRAIM is implemented after the measurement quality check or pre-processing scheme, which includes cycle slip detection algorithms. In addition, cycle slips are not considered as part of the satellite faults to be detected by the SS method in RRAIM. According to RTCA (2016), cycle slips are the responsibility of the manufacturer. In the risk allocation performed in this paper, the navigation system assumes a fault-free receiver, as per the standard approach. Therefore, the loss of signal availability due to cycle slips is not assessed in this paper.

7 | CONCLUSIONS

This paper proposes the use of a GBAS/INS+RRAIM navigation solution for surface operations under low-visibility conditions. To determine feasibility, modified accuracy and integrity requirements are provided based on recommendations in the standards and reference literature. Compliance to these requirements is examined during both the pre-coasting GBAS/INS operation and RRAIM coasting. In addition to a conventional integrity analysis, this paper proposes an approach to assess whether the surface movement requirement is met by GBAS monitoring. The results show that the accuracy and integrity requirements are easily met with non-zero values of the nominal differential bias for the rapid exit taxiway and taxiway during both pre-coasting and coasting. The integrity analysis showed that RRAIM can be initiated either on the taxi lane or on the apron with zero differential nominal bias or on the taxiway with up to 0.4 m of differential nominal bias when GAST F corrections are applied. The accuracy and integrity performance of RRAIM coasting were also assessed for all sub-phases under the assumption that coasting is initiated in each sub-phase. Three simulation scenarios, including GPS-only GAST D, GPS-only GAST F, and GPS/Galileo GAST F, were tested to evaluate the impact of DF multi-constellation processing. The requirements are met in the rapid exit taxiway and normal taxiway with a sufficient margin in the differential nominal bias for RRAIM regardless of the simulation scenario. For other sub-phases, GPS/Galileo GAST F allows a larger differential nominal bias than the other two scenarios. In terms of the integrity analysis, under a single-failure consideration, GPS/Galileo GAST F allows the largest differential nominal bias. The multiple-failure consideration allows a slightly lower differential nominal bias overall for all simulation scenarios.

From the simulation results, it can be concluded that the limiting factor is the integrity performance of the GBAS/INS pre-coasting solution. This feasibility assessment was conducted without employing any additional monitors at the airborne side, instead relying on the PMD performance of the ground monitor. If additional monitors are implemented at the airborne side, we expect that this restriction can be relaxed, consequently allowing for a larger differential nominal bias for all sub-phases. In this paper, we have conducted simulations only for surface movement after landing. For surface operations prior to take-off, convergence of the GBAS/INS solution would be required. In addition, the integrity risk is allocated to the INS failure to avoid underestimating the PL. Further work on the INS, such as a classification of INS failures and fault detection algorithms, should provide more practical results in the near future.

To conclude, the proposed approach offers a potentially feasible means to achieve low-visibility operations on the airport surface, particularly for the sub-phases following landing. This improvement may be achieved by leveraging systems that are already certified (GBAS GAST D, INS) and incorporating new techniques (GBAS/INS+RRAIM) or by utilizing mature proposed systems (GBAS GAST F, INS) with more relaxed constraints. Limitations relate to the more demanding sub-phases near the gate and the uncertainty of constraints (nominal differential bias, coasting time). However, these are practical constraints that can be resolved through further development. The major advantage of this approach is that it offers the potential for new applications without the high certification challenges posed by new sensors such as video and lidar.

ACKNOWLEDGEMENTS

This project has received funding from the SESAR Joint Undertaking under the European Union's Horizon 2020 research and innovation programme under grant agreement no. 874478.

Disclaimer: The opinions expressed herein reflect the authors' views only. Under no circumstances shall the SESAR Joint Undertaking be responsible for any use that may be made of the information contained herein.

REFERENCES

Amielh, C., Chabory, A., Macabiau, C., & Azoulai, L. (2019). GNSS multipath error model for aircraft surface navigation based on canonical scenarios for class F airports. *Proc. of the 32nd International Technical Meeting of the Satellite Division of the Institute of Navigation (ION GNSS+ 2019),* Miami, FL, 1418–1437. https://doi.org/10.33012/2019.16907

Blanch, J., Lee, Y., Pervan, B., Rippl, M., Spletter, A., & Kropp, V. (2015). Baseline advanced RAIM user algorithm and possible improvements. *IEEE Transactions on Aerospace and Electronic Systems*, *51*(1), 713–732. https://doi.org/10.1109/TAES.2014.130739

Brenner, M., & Liu, F. (2010). Ranging source fault detection performance for category III GBAS. *Proc. of the 23rd International Technical Meeting of the Satellite Division of the Institute of Navigation (ION GNSS 2010*), Portland, OR, 2618–2632. https://www.ion.org/publications/abstract.cfm?articleID=9370

Brown, R. G., & Hwang, P. Y. C. (1996). *Introduction to random signal and applied Kalman filtering* (3rd ed.). John Wiley & Sons. https://books.google.com/books/about/Introduction_to_Random_Signals_and_Appli.html?id=De9SAAAAMAAJ

Circiu, M.-S., Caizzone, S., Enneking, C., Fohlmeister, F., Rippl, M., Meurer, M., Felux, M., Gulie, I., Rüegg, D., Griggs, J., Lazzerini, R., Hagemann, F., Tranchet, F., Bouniol, P., & Sgammini, M. (2021). Final results on airborne multipath models for dualconstellation dual-frequency aviation applications. *Proc. of the 2021 International Technical Meeting of the Institute of Navigation* 714–727. https://doi.org/10.33012/2021.17862

Crassidis, J., & Junkins, J. (2004). *Optimal estimation of dynamic systems*. Capman & Hall/CRC. https://books.google.com/books?id=EeSQjQfJgkUC&printsec=copyright#v=onepage&q&f=false

European Aviation Safety Agency (EASA) (2003). *Easy access rules for all weather operations*. CS-AWO. https://www.easa.europa.eu/en/document-library/easy-access-rules/easy-access-rules-all-weather-operations-cs-awo

Federal Aviation Administration (FAA) (1999). *Criteria for approval of category III weather minima for takeoff, landing, and rollout*. AC 120-28D. https://www.faa.gov/regulations_policies/advisory_circulars/index.cfm/go/document.information/documentid/22750

Federal Aviation Administration (FAA) (2021). *Satellite navigation - GBAS - How it works*. Retrieved on September 1, 2021. https://www.faa.gov/about/office_org/headquarters_offices/ato/service_units/techops/navservices/gnss/laas/howitworks

Global Positioning System Performance Standards (GPS SPS) (2020). Department of Defense, United States. https://www.gps.gov/technical/ps/2020-SPS-performance-standard.pdf

Gratton, L., Joerger, M., & Pervan, B. (2010). Carrier phase relative RAIM algorithms and protection level derivation. *Journal of Navigation*, *63*(2), 215–231. https://doi.org/10.1017/S0373463309990403

Groves, P. D. (2013). How does non-line-of-sight reception differ from multipath interference? *Inside GNSS*, November/December issue, 40–42. https://insidegnss.com/multipath-vs-nlos-signals/

Guilbert, A. (2016). *Optimal GPS/Galileo GBAS methodologies with an application to troposphere* [Doctoral dissertation, Université de Toulouse]. https://theses.hal.science/tel-01347791

ICAO (2004). *European manual on advanced surface movement guidance and control systems*. https://store.icao.int/en/advance-surface-movement-guidance-and-control-systems-a-smgcs-manual-doc-9830

ICAO (2009). *GBAS CAT II/III development baseline SARPs*. ICAO NSP. http://www.icao.int/safety/airnavigation/documents/gnss_cat_ii_iii.pdf

ICAO (2016). *Annex 14 aerodrome design and operations* (Vol. 1). https://store.icao.int/en/annex-14-aerodromes

ICAO (2018). *Annex 10 radio navigation aids* (Vol. 1, Amendment 91). https://store.icao.int/en/annex-10-aeronautical-telecommunications-volume-i-radio-navigational-aids

Jiang, Y., Milner, C., & Macabiau, C. (2017). Code carrier divergence monitoring for dual-frequency GBAS. *GPS Solutions*, *21*(2), 769–781. https://doi.org/10.1007/s10291-016-0567-4

Khanafseh, S., Langel, S., & Pervan, B. (2010). Overbounding position errors in the presence of carrier phase multipath error model uncertainty. *Proc. of the IEEE/ION Position, Location, and Navigation Symposium (PLANS 2010),* Indian Wells, CA, 575–584. https://doi.org/10.1109/PLANS.2010.5507313

Langel, S., Crespillo, O. G., & Joerger, M. (2021). Overbounding the effect of uncertain Gauss-Markov noise in Kalman filtering. *NAVIGATION, 68*(2), 259–276. https://doi.org/10.1002/navi.419

Lee, Y. C., & McLaughlin, M. P. (2008). A position domain relative RAIM method. *Proc. of IEEE/ION Position, Location, and Navigation Symposium (PLANS 2008),* Monterey, CA, 271–284. https://doi.org/10.1109/PLANS.2008.4570016

Liu, F., Brenner, M., & Tang, C. Y. (2006). Signal deformation monitoring scheme implemented in a prototype local area augmentation system ground installation. *Proc. of the 19th International Technical Meeting of the Satellite Division of the Institute of Navigation (ION GNSS 2006),* Fort Worth, TX, 367–380. https://www.ion.org/publications/abstract.cfm?articleID=6855

Macabiau, C., Milner, C., Chabory, A., Suard, N., Rodriguez, C., Mabilleau, M., Vuillaume, J., & Hegron, S. (2015). Nominal bias analysis for ARAIM user. *Proc. of the 2015 International Technical Meeting of the Institute of Navigation*, Dana Point, CA, 713–732. https://www.ion.org/publications/abstract.cfm?articleID=12666#:~:text=A%20nominal%20bias%20is%20a,included%20in%20this%20Bnom%20parameter.

MATLAB (2021). *Simulate and track en-route aircraft in Earth-centered scenarios*. Retrieved on August 15, 2021, from https://www.mathworks.com/help/fusion/ug/simulate-and-track-en-route-air-traffic-with-earth-centered-scenarios.html

Montloin, L. (2014). *Impact of GNSS singular events on the integrity of airport navigation systems* [Ph.D. Dissertation, Université de Toulouse]. https://theses.hal.science/tel-01377380v2

Murphy, T., Harris, M., McGraw, G., Wichgers, J., Lavik, L., Topland, M., Tuffaha, M., & Saito, S. (2021). Alternative architecture for dual frequency multi-constellation GBAS. *Proc. of the 34th International Technical Meeting of the Satellite Division of the Institute of Navigation (ION GNSS+ 2021)*, St. Louis, MO, 1334–1374. https://doi.org/10.33012/2021.18152

Pervan, B., Khanafseh, S., & Patel, J. (2017). Test statistic auto- and cross-correlation effects on monitor false alert and missed detection probabilities. *Proc. of the 2017 International Technical Meeting of the Institute of Navigation*, Monterey, California, 562–590. https://doi.org/10.33012/2017.14874

Pullen, S. (2012). Augmented GNSS: Fundamentals and keys to integrity and continuity. *ION GNSS 2012 Tutorial*. https://www-leland.stanford.edu/~spullen/ION%20GNSS%202011%20Tutorial%20-%20Aug-GNSS%20final%20(Pullen,%2009-16-11).pdf

Rhee, I., Abdel-Hafez, M.-F., & Speyer, J.-L. (2004). Observability of an integrated GPS/INS during maneuvers. *IEEE Transactions on Aerospace and Electronic Systems*, *40*(2), 526–535. https://doi.org/10.1109/TAES.2004.1310002

RTCA (1999). *DO-247, The role of the GNSS in supporting airport surface operations*. https://my.rtca.org/productdetails?id=a1B36000001IcjpEAC

RTCA (2004). *DO-245, Minimum aviation system performance standards for the local area augmentation system (LAAS).* https://my.rtca.org/productdetails?id=a1B36000001IcjtEAC

RTCA (2016). *DO229, Minimum aviation system performance standards for Global Positioning System/satellite-based augmentation system airborne equipment*. https://my.rtca.org/productdetails?id=a1B3600000211rIEAQ

RTCA(2017).*DO-253D,Minimumoperationalperformancestandardsfor GPSlocalareaaugmentation system airborne equipment*. https://my.rtca.org/productdetails?id=a1B36000003Gl7ZEAS

Schuster, W., & Ochieng, W. (2011). Airport surface movement – Critical analysis of navigation system performance requirements. *Journal of Navigation*, *64*(2), 281–294. https://doi.org/10.1017/S0373463310000500

SESAR (2015). *D3.7.1, ST3.7 Threat identification and integrity allocation.*

SESAR (2021). *D9.2.120, Appendix H: Surface movement feasibility analysis.*

Stanford University (2022). *MATLAB algorithm availability simulation tool*. Retrieved on September 19, 2022, from https://gps.stanford.edu/resources/software-tools/maast

van Graas, F., & Soloviev, A. (2004). Precise velocity estimation using a stand-alone GPS receiver. *NAVIGATION*, 51(4), 283–292. https://doi.org/10.1002/j.2161-4296.2004.tb00359.x

Wallner, S., Perea, S., Odriozola, M., Brieden, P., Binder, K., Nuckelt, A., Donatelli, A., Joly, D., Stallo, C., Sgammini, M., Martini, I., Boyero, J. P., Mabilleau, M., & Canestri, E. (2021). Galileo H-ARAIM characterization and Galileo integrity support message (ISM). *Proc. of the 34th International Technical Meeting of the Satellite Division of the Institute of Navigation (ION GNSS+ 2021)*, St. Louis, MO, 1375–1391. https://doi.org/10.33012/2021.18153

Walter, T., Enge, P., Blanch, J., & Pervan, B. (2008). Worldwide vertical guidance of aircraft based on modernized GPS and new integrity augmentations. *Proceedings of the IEEE*, *96*(12), 1918–1935. https://doi.org/10.1109/JPROC.2008.2006099

Wong, G. (2014). *Impact of nominal signal deformations on satellite navigation systems* [Doctoral Dissertation, Stanford University]. https://purl.stanford.edu/wy655jp2867

Xu, G. (2007). *GPS theory, algorithms and applications*. Springer. https://doi.org/10.1007/978-3-540-72715-6

How to cite this article: Song, J., Milner, C., & No, H. (2024). Feasibility study of GBAS/INS and RRAIM for airport surface movement under low-visibility conditions. *NAVIGATION, 71*(4). https://doi.org/10.33012/navi.673

APPENDIX A

The system error defined in Equation (4) requires a time constant of multipath in the smoothed pseudorange residual of aircraft after the GBAS correction has been applied. Because GBAS reference receivers use a multipath-limiting antenna, the temporal correlation in the pseudorange residual of an aircraft primarily arises from the multipath associated with the aircraft. The autocorrelation model of multipath in a raw pseudorange for a Boeing aircraft has been derived by Pervan et al. (2017). The assessed time constant ranges from 7 s at the 5th percentile to 170 s at the 95th percentile. To obtain the range for the time constant of smoothed multipath, we conducted a Monte Carlo simulation. First, we modeled the time constant of a raw multipath as various legacy distributions with constraints at the 5th, 50th, and 95th percentiles from Pervan et al. (2017). Figure 8 shows a cumulative distribution of various models, including normal, non-central chi-square, and log-normal distributions. We chose a log-normal distribution to model the time constants of the raw multipath. As shown in Figure 8, because time constants at high percentiles are not easily modeled by legacy distributions, those at higher than the 95th percentile were generated randomly based on a uniform distribution with the maximum value set at 900 s (Langel et al., 2021). In addition, the minimum time constant was assumed to be 5 s, which is smaller than the value at the 5th percentile given by Pervan et al. (2017). A total of 10^5 time constants were generated, and for each time constant, the time history of multipath was generated via the first-order Gauss–Markov process for a time period of 2 h. Furthermore, carrier smoothing filter with a 30-s or 100-s time constant, which are used for SF and DF GBAS modes (GAST D and F), was applied. Figure 9 shows a selected number of autocorrelations of raw and smoothed multipaths. Each line of autocorrelation is color-coded according to its time constant. Table 8 summarizes the estimated time constant from the autocorrelation functions in the simulation. The time constant of generated multipath agrees well with values from the literature and the simulation conditions. Applying a smoothing filter further increases the temporal correlation of the multipath, as shown in Table 8. The obtained maximum and

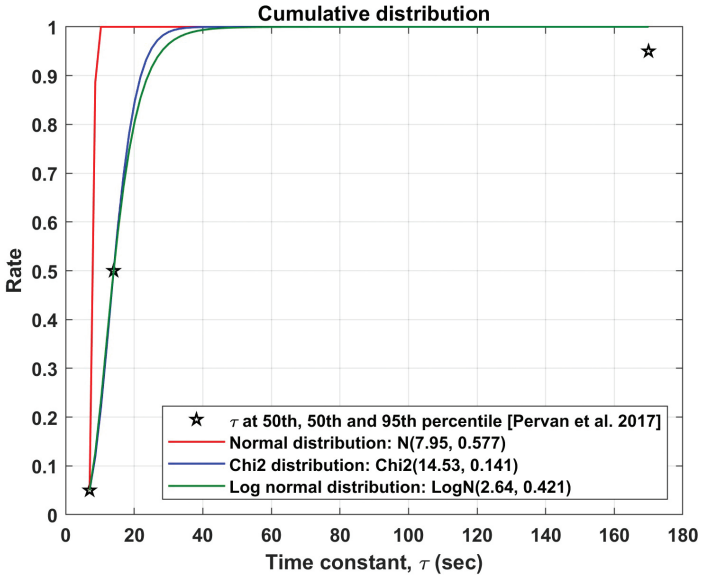

FIGURE 8 Modeling of the time constant of multipath in a raw code pseudorange based on information from Pervan et al. (2017)

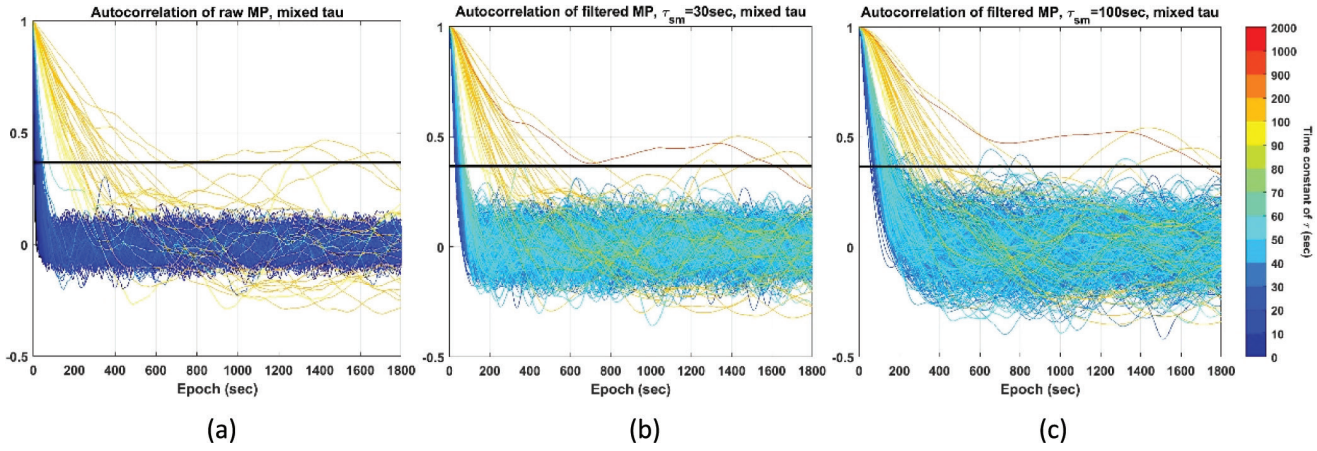

FIGURE 9 Selected autocorrelation of multipath (MP) in (a) raw code, (b) smoothed code with a smoothing time constant of 30 s, and (c) smoothed code with a smoothing time constant of 100 s

The thick black horizontal line indicates e^{-1}.

TABLE 8

Time Constants of Multipath Estimated From Simulation (τ_{sm}: Time Constant of the Carrier Smoothing Filter)

		Time constant of multipath (s)			
		Literature	Raw multipath	Smoothed multipath (τ_{sm} = 30 s)	Smoothed multipath (τ_{sm} = 100 s)
Minimum		5 (assumption)	5	26	54
Percentile	**5th**	7 (Pervan et al., 2017)	8	36	82
	50th	14 (Pervan et al., 2017)	15	48	116
	95th	170 (Pervan et al., 2017)	170	196	287
Maximum		900 (Langel et al., 2021)	899	2315	2894

minimum values of the time constant were used in the Kalman filter system error equation and to set the initial covariance of the colored noise state to ensure that the Kalman filter covariance matrix bounds the true estimate error covariance matrix (Langel et al., 2021).

APPENDIX B

The test statistics of GBAS ground monitors are temporally correlated because of temporal correlation of the inputs and the filtering effect. Therefore, we cannot consider each individual test as independent. The effective decorrelation time, $\tau_{effective}$, indicates the time interval between two tests that can be considered independent of each other. In this paper, a code-carrier divergence (CCD) monitor, excessive acceleration monitor, and Honeywell signal quality monitor (SQM) are analyzed to derive the effective decorrelation time. The term $\tau_{effective}$ is set to 100 s based on the analysis below.

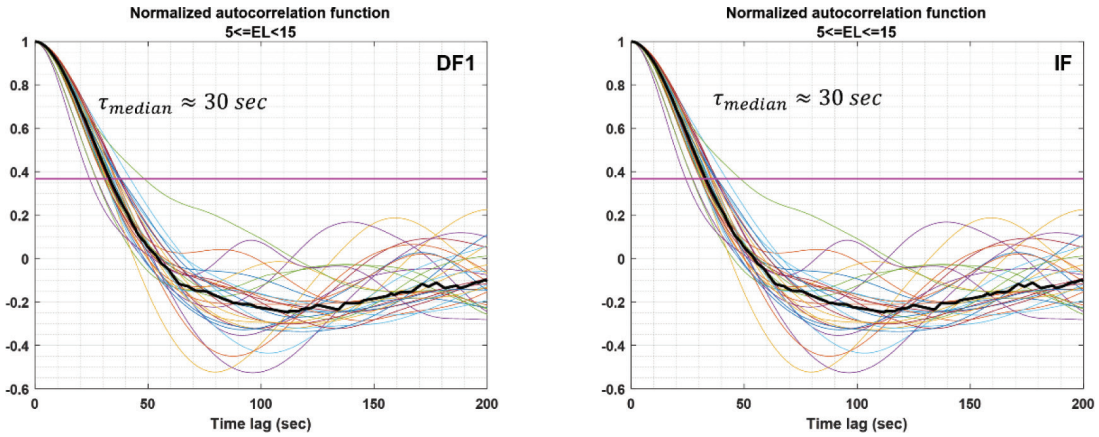

FIGURE 10 Normalized autocorrelation function of DF1 and IF CCD monitors computed for low elevation (EL) angles (horizontal magenta line: e^{-1})

B.1 | CCD Monitor

Divergence-free L1 and IF CCD monitors (Jiang et al., 2017) in GAST D and F use a two-cascade first-order filter with a time constant of 30 s. GNSS data were collected from a GBAS research prototype at the Tenerife Airport within the frame of the SESAR project for two days from day-of-year 128 with a 0.5-s sampling interval. Figure 10 shows the normalized autocorrelation functions of all test statistics at low elevation angles. The median of the normalized autocorrelation function (thick black line) becomes zero when the time lag is approximately 60 s. Thus, the effective decorrelation time for the CCD monitor is 60 s.

B.2 | Excessive Acceleration Monitor

The excessive acceleration monitor is based on the average acceleration of the carrier phase (Brenner & Liu, 2010). To compute the excessive acceleration monitor, the acceleration of satellite motion, satellite clock bias, and receiver clock bias are computed and compensated to eliminate the bias component in the estimated carrier phase acceleration. The data set used for the CCD monitor analysis is employed to compute the normalized autocorrelation function of the excessive acceleration monitor. Figure 11 shows overlapped normalized autocorrelation functions for all pseudorange noise (PRN) values at elevation angles of less than 15°. The thick black line corresponds to the median over all autocorrelation functions and approaches zero for lag times greater than 2 s. Therefore, the effective decorrelation time for the excessive acceleration monitor is 2 s.

B.3 | SQM

The Honeywell SQM used for GAST D and F (Liu et al., 2006) is considered here. Multi-correlator outputs were collected at Ecole Nationale de l'Aviation Civile (ENAC) for three days in November 2021 using IFEN SX3 software receiver with a Novatel choke-ring antenna. The correlator locations ranged from –0.05 chip to 0.1250 chip with 0.025-chip spacings, and correlator outputs with an elevation angle of less than 30° were used for the analysis.

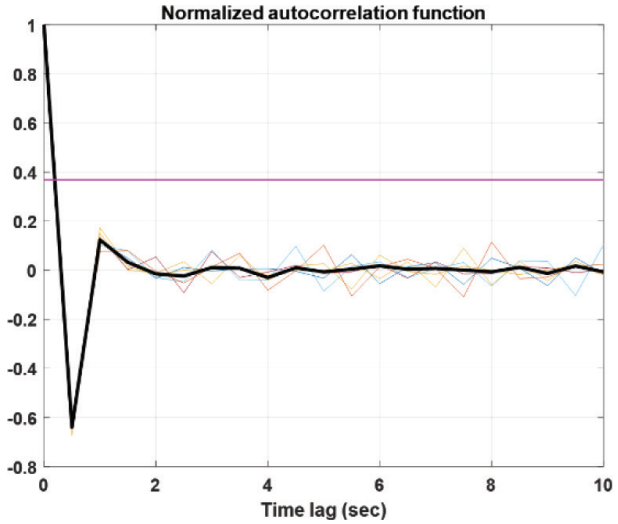

FIGURE 11 Normalized autocorrelation function of the excessive acceleration monitor (horizontal magenta line: e^{-1})

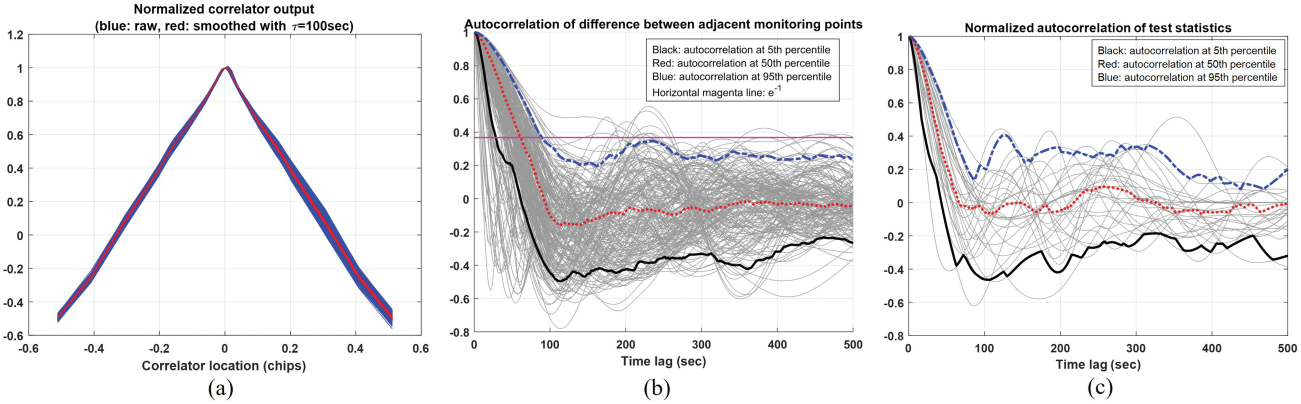

FIGURE 12 (a) Examples of correlator outputs of Galileo PRN27, (b) time histories of the difference between adjacent monitoring points used for SQM test statistics for all PRNs, and (c) autocorrelation of test statistics for all PRNs

Figure 12(a) shows an example of raw and smoothed correlator outputs with a smoothing window of 100 s. Figure 12(b) depicts the autocorrelation of the individual time series of the difference between adjacent chip locations, providing SQM test statistics. The thick black, red, and blue lines represent autocorrelations at the 5^{th}, 50^{th} and 95^{th} percentiles. The results show that most of the autocorrelation curves have a time constant of less than 100 s. Figure 12(c) represents the normalized autocorrelation of SQM test statistics, corresponding to the square sum of the residual of difference between adjacent chip locations. The results show that the test statistics become decorrelated after approximately 100 s. Based on these results, the effective decorrelation time is set to 100 s for the SQM test.